Submitted to **Journal of Hydraulic Research**, June, 2004

The Response of Turbidity Currents to a Canyon-Fan Transition: Internal Hydraulic Jumps and Depositional Signatures

SVETLANA KOSTIC & GARY PARKER
National Center for Earth-surface Dynamics, St. Anthony Falls Laboratory, University of Minnesota, Minneapolis, MN, 55414, USA

The Response of Turbidity Currents to a Canyon-Fan Transition: Internal Hydraulic Jumps and Depositional Signatures

SVETLANA KOSTIC & GARY PARKER

National Center for Earth-surface Dynamics, St. Anthony Falls Laboratory, University of Minnesota, Minneapolis, MN, 55414, USA

ABSTRACT

Turbidity currents often carve canyons into the continental slope, and then deposit submarine fans on lower slopes farther downstream. It has been hypothesized here that this slope decline can cause a turbidity current to a) undergo an internal hydraulic jump near the canyon-fan transition, and b) leave a depositional signal of this transition. These hypotheses are studied with a numerical model. Rapidly depositing turbidity currents need not undergo a hydraulic jump at a slope break. When a jump does occur, it can leave a depositional signal in terms of an upstream-facing step. A previous attempt to capture this signal failed because the current was treated as purely depositional. In the present model both sediment deposition and entrainment are included. An upstream-facing step appears when deposition dominates erosion. The step requires entrainment since the deposition rate is continuous through the jump, whereas the sediment entrainment rate is not. Therefore, the step is caused by enhanced net deposition due to reduced entrainment rate across the jump. Under certain circumstances, a single step can be replaced by a train of upstream-migrating cyclic steps, each separated by a hydraulic jump. The numerical model is verified against experiments, and then applied at field scale.

1. Introduction

Turbidity currents constitute a major mechanism for the transport of sediment brought in by rivers or littoral drift to the ocean floor. On relatively steep slopes they can be sufficiently erosive to excavate submarine canyons (e.g. Inman et al., 1976, Parker et al,. 1986, Normark & Piper, 1991). Bed slope drops off down the canyon, and eventually the canyon gives way to a submarine fan. This is shown for the Amazon canyon-fan system in Figure 1 (Pirmez, 1994; Pirmez & Imran, 2003). The Amazon Submarine Canyon has a length of about 130 km from

shelf break to canyon-fan transition, over which it has an average bed slope near 0.008. The dominant channel on the Upper Amazon Fan extends for another 430 km downstream of this transition, over which it has an average bed slope near 0.004. Submarine fans are commonly found at and beyond the transition between the continental slope and rise (Bouma et al., 1985); they parallel subaerial fans in many ways.

The point at which a submarine canyon debouches onto its associated submarine fan is generally thought to be associated with a decrease in channel slope sufficient to cause a transition from an overall net erosional environment upstream to an overall net depositional environment downstream. It has been hypothesized that the turbidity currents responsible for the genesis of the submarine canyon and fan might display an internal hydraulic jump near the slope transition (e.g. Menard, 1964; Van Andel & Komar, 1969; Mutti, 1977; Russell & Arnott, 2003).

An internal hydraulic jump is a zone of rather sharp transition such that a dense bottom flow upstream of it is supercritical (bulk Richardson number less than a value near unity; densimetric Froude number greater than a value near unity), and the same bottom flow downstream of it is subcritical (bulk Richardson number greater than a value near unity; densimetric Froude number less than a value near unity). Relatively speaking, supercritical flows are swift and thin, exerting a high shear stress on the bed, and subcritical flows are slow and thick, exerting a low shear stress on the bed. The rather abrupt drop in bed shear stress due to the jump might be expected to be evidenced in the nature of the sediment deposit left by a turbidity current in the vicinity of a hydraulic jump.

The nature of the hydraulic jump and the resultant deposits, i.e. turbidites, have been the subject of speculation as well. Menard (1964) reasoned that the development of levees bordering deep-sea channels is caused by the thickening of a turbidity current after a hydraulic jump. Van Andel & Komar (1969) interpreted the characteristics of sediment deposits in enclosed basins in terms of the hypothesized occurrence of a hydraulic jump. Mutti (1977) suggested that a turbidity currents undergoing a change in slope drops excess sand due to a hydraulic jump, thus causing characteristic turbidites just downstream. Russell & Arnott (2003) provided stratigraphic evidence for a hydraulic jump in a subaqueous glaciolacustrine fan succession in the Oak Ridges Moraine, southern Ontario, Canada. They note the following: “Erosion of large unconsolidated friable sand intraclasts was probably related to scouring in a hydraulic jump or scouring at the base of the flow and then followed by rapid deposition. The rapid dissipation of flow energy and generation of high volumes of entrained sediment some distance downflow of a hydraulic jump would have developed stratified flows, causing rapid sedimentation.” This description suggests

that one signature of a subaqueous hydraulic jump might be an upstream-facing step associated with rapid deposition downstream of the jump.

Internal hydraulic jumps associated with salinity or temperature-induced stratification have been studied extensively (e.g. Wilkinson & Wood, 1971; Stefan & Hayakawa, 1972; Wood & Simpson, 1984; Baddour, 1987; Rajaratnam et al., 1988). Internal hydraulic jumps in sediment-driven flows have received rather less attention. They remain unobserved in the field. As for observations at experimental scale, until recently only the study discussed in Garcia (1989, 1993) and Garcia & Parker (1989) specifically focused on internal hydraulic jumps of turbidity currents. (But see Lamb et al., 2004, and Toniolo, 2003 for recent experimental studies on internal hydraulic jumps in confined basins.)

The numerical model presented here is employed to investigate at experimental scale: (i) the limits on the formation of internal hydraulic jumps in turbidity currents near a slope break; and (ii) the role of internal hydraulic jumps in the mechanics of sediment deposition and erosion, and in particular whether a hydraulic jump can be inferred from the depositional record. Experimental data of Garcia (1993) are used first to calibrate and verify the numerical model. The model is then applied to various scenarios of turbidity currents developing along a sloping bed. A field-scale simulation provides insight into the characteristics of internal hydraulic jumps and associated depositional signatures resulting from generic field-scale flows.

2. Model formulation

2.1 Geometric configuration

Hydraulic jumps, internal or otherwise, are often driven by a bed slope that decreases in the streamwise direction. The change in slope does not need to be abrupt in order for a hydraulic jump to form. In the present work, however, the initial bed profile is simplified to an upstream portion with constant, positive slope joining continuously to a downstream portion that is horizontal. This bed configuration is shown in Figure 2. The abrupt decrease in slope increases the likelihood of a hydraulic jump occurring in the computational domain. The sloping upstream portion represents a loose surrogate for a submarine canyon, and the horizontal downstream portion is a loose surrogate for a submarine fan or abyssal plain.

The width of the turbidity current is assumed to be constant in the present work. In the field, a turbidity current debouching from a confined canyon onto an unchannelized fan can be expected to expand laterally. The effect of this expansion is not included here. In point of fact, many submarine fans are traversed by distinct, well-formed channels (e.g. Pirmez, 1994) which can act to limit lateral spread as the turbidity current forms a hydraulic jump.

2.2. Governing equations

The relations used here to describe the development of an unsteady, one-dimensional turbidity current emanating from a submarine canyon and debouching onto a submarine fan are based on the original single-layer, depth-averaged model of Parker et al. (1986). They involve integral statements of conservation of: water mass, downslope momentum, suspended sediment in the water column and bed sediment, expressed in the following respective dimensionless forms (Kostic & Parker, 2003a, 2003b).

$$\frac{\partial \hat{h}}{\partial \hat{t}} + \frac{\partial \hat{U}\hat{h}}{\partial \hat{x}} = e_w \hat{U} \tag{1}$$

$$\frac{\partial \hat{U}\hat{h}}{\partial \hat{t}} + \frac{\partial \hat{U}^2\hat{h}}{\partial \hat{x}} = -\frac{Ri_0}{2}\frac{\partial \hat{C}\,\hat{h}^2}{\partial \hat{x}} - Ri_0\hat{C}\,\hat{h}\frac{\partial \hat{\eta}}{\partial \hat{x}} - \hat{u}_*^2 \tag{2}$$

$$\frac{\partial \hat{C}\hat{h}}{\partial \hat{t}} + \frac{\partial \hat{C}\hat{U}\hat{h}}{\partial \hat{x}} = \hat{v}_s\left(\frac{e_s}{C_0} - r_0\,\hat{C}\right) \tag{3}$$

$$\frac{\partial \hat{\eta}}{\partial \hat{t}} = \frac{\hat{v}_s}{(1-\lambda)}\left(r_0\,C_0\,\hat{C} - e_s\right) \tag{4}$$

The turbidity current is driven by excess density due to suspended sediment. The suspension is assumed to be sufficiently dilute to allow the use of the Boussinesq approximation in the equation of motion (2), and to neglect the effect of hindered settling. The deposition of suspended sediment on the bed and the erosion of bed sediment are assumed to occur concomitantly. The Exner equation (4) describing the channel bed evolution is fully coupled with the parts of the model describing hydrodynamics and suspended sediment transport. The dimensionless parameters in equations (1)–(4) are defined below.

In the above relations $\hat{t}$ is dimensionless time, $\hat{x}$ is a dimensionless bed-attached streamwise coordinate, $\hat{u}_*$ denotes the dimensionless shear velocity, and $\hat{v}_S$ denotes the dimensionless fall velocity of sediment, given by the respective relations

$$\hat{x} = \frac{x}{h_0}, \quad \hat{t} = \frac{t}{h_0/U_0}, \quad \hat{u}_* = \frac{u_*}{U_0}, \quad \hat{v}_S = \frac{v_S}{U_0} \tag{5a}$$

where x, t, u_* and v_S are the corresponding variables in dimensional form. In addition λ denotes bed porosity, and r_0 is a dimensionless parameter relating the near-bed suspended sediment concentration to the layer-averaged value, here taken to be a multiplicative constant for simplicity. The dimensioned dependent variables are the current depth h, the depth-averaged

velocity U, the depth-averaged volumetric concentration of suspended sediment C, and the bed elevation η; their corresponding dimensionless forms $\hat{h}, \hat{U}, \hat{C}$ and $\hat{\eta}$ are defined as

$$\hat{h} = \frac{h}{h_0}, \quad \hat{U} = \frac{U}{U_0}, \quad \hat{C} = \frac{C}{C_0}, \quad \hat{\eta} = \frac{\eta}{h_0} \tag{5b}$$

where h_0, U_0, C_0 are the values of h, U and C at the upstream boundary (near the head of the submarine canyon). Ri_0 is the inflow bulk Richardson number, given as

$$Ri_0 = \frac{RgC_0h_0}{U_0^2} \tag{6}$$

where R denotes the submerged specific gravity of sediment, i.e. 1.65 for natural quartz.

Shear velocity is related to layer-averaged flow velocity according to the following friction relation;

$$\hat{u}_*^2 = c_D \hat{U}^2 \tag{7}$$

where c_D is a dimensionless friction coefficient.

The fall velocity v_S is calculated from the relation of Dietrich (1982), which can be expressed as

$$R_f = f\left(Re_p\right) \tag{8a}$$

where

$$R_f = v_S \Big/ \sqrt{RgD}\,, \quad Re_p = \sqrt{RgD}\; D \Big/ \nu \tag{8b}$$

Here R_f is a dimensionless particle fall velocity (not to be confused with $\hat{v}_S$), Re_p denotes a particle Reynolds number, D is a characteristic grain size of the sediment, and ν denotes the kinematic viscosity of water.

The dimensionless parameter e_w characterizes the rate of entrainment into the turbidity current of ambient water from above. The following form is used for e_w (e.g. Fukushima et al., 1985);

$$e_w = \frac{0.00153}{0.0204 + Ri_0 \dfrac{\hat{C}\hat{h}}{\hat{U}^2}} \tag{9}$$

The dimensionless parameter e_S describes the rate of sediment entrainment into suspension by a turbidity current. Two formulations are used here. The formulation used at experimental scale is that of Garcia & Parker (1991, 1993):

$$e_S = \frac{aZ^5}{1+\frac{a}{0.3}Z^5} \tag{10a}$$

where

$$Z = \alpha_1 \frac{\hat{u}_*}{\hat{v}_S} Re_p^{\alpha_2} \tag{10b}$$

In the above relations the constant a is equal to $1.3\text{x}10^{-7}$, and the constants α_1 and α_2 are given as

$$(\alpha_1, \alpha_2) = \begin{cases} (0.586, 1.23), & \text{Re}_p \le 2.36 \\ (1.0 \quad , 0.6\ ), & \text{Re}_p > 2.36 \end{cases} \tag{10c}$$

The formulation of Garcia & Parker (1991, 1993) was developed with laboratory data and tested with field data for relatively small rivers. Recently Wright & Parker (in press) have modified the formulation to cover the full range of field-scale rivers. This latter formulation is here extended with information from Garcia & Parker (1993), and further adapted for application to turbidity currents at field scale;

$$e_S = p\frac{aZ^5}{1+\frac{a}{0.3}Z^5} \tag{11a}$$

where a is now equal to $7.8\text{x}10^{-7}$,

$$Z = \alpha_1 \frac{\hat{u}_*}{\hat{v}_s} Re_p^{\alpha_2} S_f^{0.08} \tag{11b}$$

and S_f denotes a friction slope, evaluated for the case of turbidity currents from the relation

$$S_f = \frac{c_D}{Ri_o}\frac{\hat{U}^2}{\hat{C}\hat{h}} \tag{11c}$$

The adaptation used here concerns the coefficient p, which is used to characterize the degree of bed sediment strength, i.e. ability of the bed sediment to resist erosion. The entrainment formulations of Garcia & Parker (1993) and Wright & Parker (in press) are based on field data for rivers and laboratory data for rivers and turbidity currents for which the bed consists of loose, non-cohesive sediment. In the deep-water setting, however, it is common for muddy, and even sandy bed sediments to develop some degree of strength associated with consolidation. This strength is often expressed in terms of numerous muddy layers sandwiched in between sandy layers. As a result, marine sediments often cannot be treated as loose, non-cohesive material. The coefficient p includes this effect in a simple way; it is a free variable which takes the value unity for completely non-cohesive, loose material, and takes a value below unity when the bed

material is assumed to have developed strength through consolidation. In the calculations at field scale presented here p is set equal to values less than or equal to unity.

An algebraic specification for the friction coefficient c_D in (7) results in the "three-equation" formulation of Parker et al. (1986), where the three equations in question are the ones that describe flow and sediment dynamics, e.g. (1), (2) and (3). These relations admit self-accelerating, or "ignitive" solutions, according to which a sufficiently swift flow entrains ever more sediment from the bed, so becoming ever swifter (Pantin, 1979; Parker, 1982). Fukushima et al. (1985) and Parker et al. (1986) showed that this self-acceleration can result in such high rates of consumption of turbulent kinetic energy as sediment is entrained from the bed that flow becomes dynamically impossible. They overcame this problem by adding one more equation describing the evolution of layer-averaged turbulent kinetic energy. This equation takes the dimensionless form:

$$\frac{\partial \hat{K}\hat{h}}{\partial \hat{t}}+\frac{\partial \hat{U}\hat{K}\hat{h}}{\partial \hat{x}}=\hat{u}_*^2\hat{U}-\frac{1}{2}e_w\hat{U}^3-\beta\hat{K}^{3/2}-Ri_0\hat{h}\left[\hat{C}\left(\hat{v}_S+\frac{1}{2}e_w\hat{U}\right)+\frac{\hat{v}_S}{2}\left(\frac{e_S}{C_0}-r_0\hat{C}\right)\right] \tag{12}$$

In the above relation

$$\hat{K}=\frac{K}{U_0^2} \tag{13}$$

where K denotes the layer-averaged kinetic energy of the turbulence per unit mass.

Self-acceleration leads to ever-increasing values of the sediment entrainment coefficient e_S in (12). This sediment entrainment is accomplished by turbulence, and as can be seen from (12), results in a loss of turbulent kinetic energy as this energy is consumed in increasing the potential energy of the sediment so entrained. In order to dynamically link the energetics of the flow described by (12) with the sediment entrainment relations (10) or (11), it is necessary to modify the closure hypothesis (7) to the form

$$\hat{u}_*^2=\alpha\hat{K} \tag{14}$$

where α is a dimensionless coefficient to be specified algebraically. This relation specifically links the shear velocity, and thus the sediment entrainment rate, with the balance of turbulent kinetic energy. If the entrainment coefficient e_S becomes too high, $\hat{K}$ is decreased in accordance with (12), which in turn reduces $\hat{u}_*$ and thus e_S in accordance with (14) and (10) or (11), respectively. Parker et al. (1986) refer to the formulation of the flow dynamics described by (1), (2), (3) and (12) as the "four-equation" model.

The term β in (12) describes the dissipation of turbulent kinetic energy by viscosity; Parker et al. (1986) specify the following form for it:

$$\beta = \frac{\frac{1}{2} e_w \left(1 - Ri_0 \frac{\hat{C}\hat{h}}{\hat{U}^2} - 2\frac{c_D^*}{\alpha} \right) + c_D^*}{\left(\frac{c_D^*}{\alpha} \right)^{\frac{3}{2}}} \tag{15}$$

where c_D^* is a prescribed parameter that may be equated numerically to the value of c_D in the "three-equation" model. It is important to realize, however, that the value of c_D itself in the "four-equation" model is not a prescribed parameter, but is given from (7) and (14) as

$$c_D = \frac{u_*^2}{U^2} = \alpha \frac{K}{U^2} \tag{16}$$

In all calculations performed here α is set equal to 0.1, a value suggested by Parker et al. (1986).

The laboratory-scale flows simulated below are all highly depositive and show no tendency toward self-acceleration. As a result, these are adequately treated with the "three-equation" model of the flow and the sediment entrainment formulation of (10). The self-accelerational regime is specifically included in the simulations at field scale, so that both the "three-equation" and "four-equation" formulations for hydrodynamics and suspended sediment are used in the calculations, along with the sediment entrainment formulation of (11). Both formulations are dynamically coupled with the Exner equation, i.e. (4), to capture the bed evolution of a submarine canyon-fan system in response to net sediment deposition from the current.

2.3. Governing dimensionless parameters

An inspection of the "three-equation" formulation of (1-10) reveals that any characteristic parameter N of the turbidity current flow field can be expressed as a function of the following dimensionless parameters:

$$N = f\left(Ri_0, Re_p, v_S/U_0, u_*/v_S, c_D, r_0, C_0, \lambda, S_i, p \right) \tag{17a}$$

where S_i denotes the initial bed slope of the upstream portion of the domain (i.e. the submarine canyon). In accordance with the problem at hand, the analysis is restricted to underflows that are supercritical at the inflow boundary, i.e. $Ri_0 < 1$. At field scale, turbidity currents may also be expected to be supercritical as they move down a relatively steep submarine canyon (e.g. Komar, 1971). The coefficient of bed drag c_D is in general a function of a turbidity current depth. For one-dimensional turbidity currents with Reynolds number in the range $[4 \cdot 10^2, 2 \cdot 10^6]$ this coefficient can be inferred to take a value between 10^{-3} and 10^{-1} (Parker et al., 1987). The multiplicative constant r_0 defines a ratio of the near-bed volumetric concentration of suspended

sediment to the corresponding layer-averaged value. Garcia (1989) has inferred values of r_0 ranging from 1 to above 2 based on experiments on turbid underflows. A range of values for bed porosity λ is 0.2 – 0.8; porosity influences deposit thickness exclusively, without having any effect on the flow field or depositional signature. In relation (17a), the dimensionless shear velocity u_*/v_S is replaced by the ratio $\Delta u_*/v_S$, where Δu_* is an estimate of the drop in shear velocity due to the transition in the flow regime associated with the hydraulic jump, as defined in more detail below. Also, the particle Reynolds number Re_p can be replaced by the particle fall velocity R_f. In the "four-equation" formulation of (1-9) and (11-16) the parameter c_D is replaced with its equivalent c_D^*, and the parameter α must be added to the list. Therefore, the dimensionless parameters governing development of a turbidity current near a sharp canyon-fan transition are as follows:

$$N = f\left(Ri_0, R_f, v_S/U_0, \Delta u_*/v_S, c_D, r_0, C_0, S_i, p\right) \tag{17b}$$

in the "three-equation" formulation, and

$$N = f\left(Ri_0, R_f, v_S/U_0, \Delta u_*/v_S, c_D, r_0, C_0, S_i, p, c_D^*, \alpha\right) \tag{17c}$$

in the "four-equation" formulation.

2.4. Numerical formulation

The modeling of turbidity currents developing along a sloping bed involves hyperbolic governing equations and one downstream-propagating boundary (i.e. the head of the current). To cope with the latter, a deforming grid approach is adopted, and the moving boundary is fixed by means of a Landau transformation (Crank, 1984), such that the current front head is at the fixed point $x^* = 1$:

$$\begin{cases} x^* = \dfrac{\hat{x}}{\hat{s}(t)}; & \tau = \hat{t} \end{cases} \tag{18}$$

The parameter $\hat{s}$ has one of three definitions depending upon the model execution. The base definition is the dimensionless position of the turbidity current head, in which case no outflow is allowed beyond $x^* = 1$. In some implementations, however, $\hat{s}$ needs to be fixed in space, so that outflow is allowed beyond $x^* = 1$. This condition occurs, for example, when the head of the turbidity current has flowed beyond the downstream end of the computational domain. The value of $\hat{s}$ is then either matched to the dimensionless length of the computational domain (e.g. an experimental flume), or determined in terms of a specified target concentration $\hat{C}_t$ (e.g. 0.1 % of $\hat{C}_0$).

After introducing the conservative dimensionless variables $\hat{q} = \hat{U}\hat{h}$ and $\hat{\phi} = \hat{C}\hat{h}$, and applying the transformation of Eq. (18), (1)-(3) of the "three-equation" model and (4) may be written in the following conservative form:

$$\frac{\partial \hat{h}}{\partial \tau} = \frac{1}{\hat{s}}\left(x^* \hat{s} \frac{\partial \hat{h}}{\partial x^*} - \frac{\partial \hat{q}}{\partial x^*} \right) + \frac{0.00153 \dfrac{\hat{q}}{\hat{h}}}{0.0204 + Ri_0 \dfrac{\hat{\phi}\hat{h}^2}{\hat{q}^2}} \tag{19}$$

$$\frac{\partial \hat{q}}{\partial \tau} = \frac{1}{\hat{s}}\left[x^* \hat{s} \frac{\partial \hat{q}}{\partial x^*} - \frac{\partial}{\partial x^*}\left(\frac{\hat{q}^2}{\hat{h}} + \frac{Ri_0}{2}\hat{\phi}\hat{h} \right) \right] + Ri_0 \hat{\phi} \frac{\partial \hat{\eta}}{\partial x^*} - c_D \frac{\hat{q}^2}{\hat{h}^2} \tag{20}$$

$$\frac{\partial \hat{\phi}}{\partial \tau} = \frac{1}{\hat{s}}\left[x^* \hat{s} \frac{\partial \hat{\phi}}{\partial x^*} - \frac{\partial}{\partial x^*}\left(\frac{\hat{\phi}\hat{q}}{\hat{h}} \right) \right] + \hat{v}_s \left(\frac{e_s}{C_0} - r_0 \frac{\hat{\phi}}{\hat{h}} \right) \tag{21}$$

$$\frac{\partial \hat{\eta}}{\partial \tau} = \frac{x^* \hat{s}}{\hat{s}} \frac{\partial \eta}{\partial x^*} + \frac{\hat{v}_s}{(1-\lambda)}\left(r_0 C_0 \frac{\hat{\phi}}{\hat{h}} - e_s \right) \tag{22}$$

The set (19)-(22) with (10a-c) or (11a-c) comprise the essential formulation of the morphodynamic problem using the "three-equation" model of flow dynamics. The problem is solved numerically for the four unknowns: $\hat{h}, \hat{U}, \hat{C}$ and $\hat{\eta}$.

Initial conditions include an initial bed profile interpolated to the grid $0 \le x^* \le 1$. While the numerical model allows for arbitrary initial bed profile, the central case of interest is one consisting of an upstream region with constant, finite slope and a downstream region with vanishing slope. Furthermore, primitive variables $\hat{h}$, $\hat{U}$ and $\hat{C}$ are set equal to 1 at all nodal points within the initially specified length of propagation of the turbidity current $\hat{s}$.

Boundary conditions are set by means of characteristic velocities for the flow, defined as

$$c_1 = \frac{-x^* \hat{s}}{\hat{s}}, \quad c_2 = \frac{\hat{U} - x^* \hat{s}}{\hat{s}}, \quad c_{3,4} = \frac{\left(\hat{U} - x^* \hat{s}\right) \pm \sqrt{Ri_0 \hat{h} \hat{C}}}{\hat{s}} \tag{23a-d}$$

where c_1 is the velocity resulting from the transformation of the coordinate system, c_2 defines the rate at which particles are advected by the flow and $c_{3,4}$ correspond to the forward- and backward-propagating wave speeds for the underflow analogs of shallow-water waves, respectively. Inspection of the characteristic velocities of Eqs. (23a-d) reveals the following.

For a supercritical inflow boundary three characteristics propagate into the flow domain, and thus the corresponding dependent variables must be specified. They are defined as

$$\hat{h}\left(x^* = 1, \tau\right) = 1, \quad \hat{U}\left(x^* = 1, \tau\right) = 1, \quad \hat{C}\left(x^* = 1, \tau\right) = 1 \tag{24a-c}$$

At the outflow boundary the number of physical conditions is dependent upon the definition of the parameter $\hat{s}$. If the propagation of a turbidity current head is of interest (recall that $\hat{s}$ denotes the position of the head), two boundary conditions need to be imposed, independently of whether the outflow boundary is subcritical or supercritical. In the model, the velocity of the last grid point is determined from the front velocity $\hat{\dot{s}}$, and its bed elevation is determined from the antecedent bed profile $\hat{\eta}_i$, such that:

$$\hat{U}\left(x^* = 1, \tau\right) = \hat{\dot{s}} = \frac{d\hat{s}}{d\tau} \tag{25a}$$

$$\hat{\eta}\left(x^* = 1, \tau\right) = \hat{\eta}_i\left(\hat{s}\right) \tag{25b}$$

Once the turbidity current reaches some distance $\hat{L}$ (defined in terms of a specified target concentration $\hat{C}_t$ or the length of the computational domain), no physical boundary condition is required for an outflow boundary, unless a downstream control is imposed there. In the experiments of Garcia (1993) simulated here, the flume ended in a free outfall. Thus, the underflow depth at the last grid point is equated to the critical depth corresponding to a bulk Richardson number of unity, such that

$$\hat{h}\left(x^* = 1, \tau\right) = \frac{\hat{U}\left(x^* = 1, \tau\right)^2}{Ri_0\, \hat{C}\left(x^* = 1, \tau\right)} \tag{25c}$$

The remaining variables are obtained from the flow field by means of first order extrapolation (Hirsch, 1990).

The governing Eqs. (19)-(22), with the initial and boundary conditions of Eqs. (24)-(25) are solved using the QUICKEST method (Leonard, 1979), which is an explicit third-order accurate algorithm designed for highly advective unsteady flows. Unphysical overshoots and undershoots associated with a hydraulic jump and the physical condition (25a) are clipped by the ULTIMATE limiter (Leonard, 1991). The computational efficiency of the scheme is significantly improved by the introduction of time stretching accompanying grid stretching, thus maintaining the Courant number. A more comprehensive discussion of the numerical method can be found in Kostic & Parker (2003a). The physics of the present model, however, differ from those in the submodel of Kostic & Parker (2003a) pertaining to turbidity currents in two important ways; a)

the present model allows for entrainment of bed sediment by the turbidity current, whereas the flows of Kostic & Parker (2003a) are purely depositional, and b) Kostic & Parker (2003a) allow for partial driving of the underflow due to temperature stratification, whereas the present model does not.

Since the above model based on the "three-equation" formulation is very similar to the model of Kostic & Parker (2003a), it is of use to note the following. The present numerical model is verified using the experiments of Garcia (1989), as discussed below. The model of Kostic & Parker (2003a) was verified by means of the experiments reported in Kostic (2001) and Kostic & Parker (2003b), which were conducted in the same facility as, and were in many ways similar to those of Garcia (1989). The main difference is that the experiments of Kostic (2001) and Kostic & Parker (2003b) included a self-formed delta from which a plunging turbidity current formed.

The extension to the "four-equation" model of flow dynamics is straightforward; (19), (21) and (22) are unaltered, (20) is amended to

$$\frac{\partial \hat{q}}{\partial \tau} = \frac{1}{\hat{s}}\left[x^* \hat{s} \frac{\partial \hat{q}}{\partial x^*} - \frac{\partial}{\partial x^*}\left(\frac{\hat{q}^2}{\hat{h}} + \frac{Ri_0}{2}\hat{\phi}\hat{h} \right) \right] + Ri_0 \hat{\phi} \frac{\partial \hat{\eta}}{\partial x^*} - \alpha \frac{\hat{\varpi}}{\hat{h}} \tag{26}$$

and (12) is transformed with (18) to

$$\frac{\partial \hat{\varpi}}{\partial \tau} = \frac{1}{\hat{s}}\left[x^* \hat{s} \frac{\partial \hat{\varpi}}{\partial x^*} - \frac{\partial}{\partial x^*}\left(\frac{\hat{\varpi}\hat{q}}{\hat{h}} \right) \right] + \alpha\left(\frac{\hat{\varpi}\hat{q}}{\hat{h}^2} \right) - \frac{0.000765\left(\frac{\hat{q}}{\hat{h}} \right)^3}{0.0204 + Ri_0 \frac{\hat{\phi}\hat{h}^2}{\hat{q}^2}} - \beta\left(\frac{\hat{\varpi}}{\hat{h}} \right)^{3/2} +$$
$$- Ri_0 \left[\hat{\phi}\left(\hat{v}_S + \frac{0.000765 \frac{\hat{q}}{\hat{h}}}{0.0204 + Ri_0 \frac{\hat{\phi}\hat{h}^2}{\hat{q}^2}} \right) + \frac{\hat{v}_S}{2}\left(\frac{e_S \hat{h}}{C_0} - r_0 \hat{\phi} \right) \right] \tag{27}$$

where $\hat{\varpi}$ is a new conservative dimensionless variable defined as $\hat{\varpi} = \hat{K}\hat{h}$

The initial condition for $\hat{K}$ is set in the same way as for $\hat{h}$, $\hat{U}$ and $\hat{C}$; i.e. $\hat{K}$ is set equal to 1 at all nodal points within the initially specified length of propagation of the turbidity current $\hat{s}$.

3. **Verification of the numerical model**

3.1. Experiments of Garcia (1989) on hydraulic jumps near a slope transition

The numerical model using the "three-equation" dynamic formulation was validated using an experimental study conducted by Garcia (1989) to elucidate the behavior of continuous, saline and turbidity currents near a canyon-fan transition. The sediment entrainment formulation in all

simulations at experimental scale, both in this section and in Section 4, is that of Eqs. (10a-10c); i.e. that of Garcia & Parker (1991, 1993). The bed is assumed to be freely erodible.

Results pertaining to the experiments of Garcia (1989) are also reported in Garcia (1993) and Garcia & Parker (1989). For the sake of brevity, these three papers are referred to as "GGGP" below. The experimental flume was 30 cm wide and 70 cm deep. A submarine canyon was modeled by a 5 m long inclined bed with a slope S_i of 0.08 ($\theta = 4.6^0$), followed by a 6.6 m long horizontal bed that represented the associated abyssal plain (Figure 2). A free outfall at the end of the horizontal region acted as a downstream control. The currents were allowed to develop until a quasi-steady state continuous flow was reached.

The experimental program included conservative saline currents, turbidity currents driven by well-sorted sediment, turbidity currents driven by poorly-sorted sediment, and sediment-entraining saline currents. Of particular interest in regard to the analysis at hand are experiments reported in GGGP on internal hydraulic jumps in underflows driven by well-sorted sediment.
The most important conclusions of these experiments can be summarized as follows:

(1) Saline hydraulic jumps and jumps in fine-grained turbidity currents have similar characteristics.
(2) The amount of water entrained by the flow while going through a hydraulic jump is small. Most of the water entrainment takes place in the jet-like, supercritical region before the jump, while the entrainment in the plume-like, subcritical regime is negligible. This observation is in line with the conclusions on the dilution of heated water discharges at relatively low Richardson number (Wilkinson & Wood, 1971; Stefan & Hayakawa, 1972; Baddour, 1987).
(3) The strength of an internal hydraulic jump, quantified by the ratio of the current thickness after the jump to that before it, is seen to take values similar to those predicted by the relation of Yih & Guha (1955) for jumps in stratified flows.
(4) The most significant effect of the slope transition on the flow characteristics is the marked reduction of bed shear stress downstream of the hydraulic jump. Garcia (1993) reports that the break in slope did not seem to cause any discontinuity in the depositional pattern of the currents capable of reaching the downstream end of the flume. It is indicated below, however, that a very weak discontinuity is observable in at least one of the experiments.
(5) There is a clear correlation between deposit thickness and grain size of the sediment driving the flow. For similar inlet conditions, the coarser sediment generates a thicker proximal deposit that tapers more rapidly downstream. The thickness of a deposit decreases roughly exponentially with distance from the inlet.

Table 1 lists the inlet conditions for the numerical simulations of a selection of the experiments of GGGP on hydraulic jumps near a canyon-fan transition. Additional input parameters include bed friction coefficient c_D = 0.01 and bed porosity $\lambda = 0.5$. In all cases the time of simulation was equal to the run time of the experiment itself. In addition, the parameter p

3.2 Test of the numerical model

The central focus of the experiments reported in GGGP is on the depositional pattern set up by quasi-steady-state turbidity currents undergoing an internal hydraulic jump; data pertaining to the early-stage setup of quasi-steady-state flow are not available. Under quasi-steady-state conditions the current is continuous and the flow changes only very slowly due to the slowly changing bed configuration induced by sediment deposition.

A numerical model must not only capture this quasi-steady condition, however, but also the more strongly time-dependent process by which this condition is set up. That is, it must in addition capture a) the propagation of the front out of the domain, b) the initial and time-evolving response of the current to the break in slope and c) the setup of the internal hydraulic jump.

In order to demonstrate that the numerical model reported here can indeed capture these features, simulations are performed using the experimental conditions of run NOVA1 reported in Garcia (1989). Choi & Garcia (1995) used the conditions of run NOVA1 to demonstrate the ability of their numerical model to capture the salient features of time-evolving turbidity currents near slope breaks; these conditions are used to the same end here. In the calculations presented here r_o is set equal to unity.

Run NOVA1, which employed a sediment with a characteristic size D of 4 μm, was continued for 2400 s (40 minutes). The first 18 minutes of the run were consumed by the setup of a quasi-steady-state flow. During this early period the front of the turbidity current ran out to the end of the tank and flowed over an invert into a larger damping tank, and a distinct hydraulic jump near the slope break gradually came into being.

The predictions of the numerical model can be characterized in terms of a) the elevation ξ of the interface between the turbidity current and the ambient water above, given as

$$\xi = \eta + h \tag{28}$$

and b) the densimetric Froude number Fr_d, where Fr_d and the corresponding bulk Richardson number Ri are defined as

$$Fr_d = \frac{U}{\sqrt{RgCh}} \quad , \quad Ri = Fr_d^{-2} = \frac{RgCh}{U^2} \tag{29a,b}$$

These predictions are shown in Figure 3a (elevation of the interface between the turbidity current and the ambient water above) and Figure 3b (densimetric Froude number). As the underflow hits the break in slope, it decelerates considerably, and therefore thickens. Time is required, however, for this thickening to sharpen into a distinct hydraulic jump. After a quasi-steady flow is set up, it changes in time only in response to the gradual deposition of sediment on the bed. The numerical model predicts a distinct hydraulic jump with a clear transition from supercritical ($Fr_d > 1$ or $Ri < 1$) to subcritical flow ($Fr_d < 1$ or $Ri > 1$) well before the end of the run, as seen in Figures 3a and 3b. The results shown therein are not greatly different from those shown in Choi & Garcia (1995).

In Figures 4a,b the present model is tested against experimental data from run NOVA2 of GGGP for layer-averaged concentration C, layer-averaged flow velocity U and the elevation ξ of the interface between turbid and clear water. The run in question again employed material with a characteristic grain size of 4 μm. The duration of the run was 40 minutes; input data are given in Table 1. Shown in Figure 4a are measured data for ξ versus streamwise distance x; Figure 4b shows U and C versus x. These data were taken toward, but not precisely at the end of the run.

Also shown in Figures 4a and 4b are corresponding numerical results from the predictions of the present model at the end of the run, as well as those reported in Choi & Garcia (1995). In general the both the present model and that of Choi & Garcia (1995) fit the data reasonably well. A point of difference is that the measured hydraulic jump in Figures 4a and 4b appears to be more diffuse than that predicted numerically. This is likely simply due to the fact that in a layer-averaged approach, a hydraulic jump is manifested as a shock, whereas in reality the jump is dispersed over a streamwise length corresponding to a few current thicknesses.

The present model differs from that of Choi & Garcia (1995) in one important way; the dimensionless sediment entrainment rate e_s is retained in the present model, but dropped in that of Choi & Garcia (1995). It will be shown below that retention of this term is essential in order to predict a depositional signal of an internal hydraulic jump. In the event, for the conditions of run NOVA1 and NOVA2 entrainment was found to play a negligible role in the present model, so justifying *a posteriori* the assumption used by Choi & Garcia (1995) to model these runs.

Garcia (1993) specifically notes that "the turbidity currents driven by 4 μm sediment showed little tendency to deposit either in the model canyon or on the model fan…" The present numerical model is in agreement with this observation, predicting negligible deposition of sediment anywhere in the simulations of runs NOVA1 and NOVA2.

In addition to the runs NOVA1 and NOVA2 conducted with 4 μm sediment, also included in Table 1 are the GGGP runs DAPER1, DAPER4 and DAPER7 conducted with 9 μm sediment,

runs GLASSA2, GLASSA5 and GLASSA7 conducted with 30 μm sediment, and runs GLASSB1, GLASSB2 and GLASSB3 conducted with 65 μm sediment. These experiments were simulated with the present model in order to test numerical predictions against experimental data for deposit thickness per unit bed area; the results are summarized below.

Figures 5a, 6a and 7a illustrate the measured and computed streamwise variation in sediment mass deposited per unit bed area by turbidity currents driven by 9, 30 and 65 μm sediment respectively. Both the observations and calculations pertain to the end of each run. The best fit with experimental observations was attained with $r_0 = 1$ for the runs with 9 and 30 μm sediment, while for the currents with 65 μm sediment r_0 is set equal to 2. These choices appear reasonable, since the sediment concentration profiles of fine-grained underflows show a tendency to be more uniformly distributed in the vertical. The agreement between the experimental data and the present numerical model is generally very good.

The deposits generated by 9 μm currents were weakly depositional, having almost uniform thickness along the model canyon and fan. On the other hand, 30- and 65-μm currents created deposits that were strongly depositional, and displayed roughly exponential decreases in thickness with distance from the sediment source. According to GGGP, the break in slope did not seem to cause any discontinuity in the depositional pattern of those currents which were capable of reaching the downstream end of the fan. Yet, the numerical simulations of experiments that involved an internal hydraulic jump reveal a modest but clear depositional step associated with a drop in shear stress right after the jump. That is, the deposit thickens from the upstream to the downstream side of the jump. For example, in the case of run DAPER4 the simulated deposit mass per unit bed area showed an increase of 0.0053 g/cm^2 across the jump, and for run DAPER7 the increase was 0.076 g/cm^2.

It is value to ask whether or not any such depositional signal was observed in the data. The only run that seems to show this increase is run DAPER 7 (Figure 5a), where the step (denoted with an arrow, and illustrated more clearly in an inset) is near the predicted size. In the case of run DAPER 4, the predicted step is sufficiently small that even if real it would not have been clearly seen in the data. There is no evidence of a depositional signal in the data for the 30 μm and 65 μm sediment. The data and numerical results for run DAPER7 thus provide the first hint that under the right conditions a hydraulic jump might leave a depositional signal. The issue is addressed with further numerical experiments below.

Figures 5b, 6b and 7b show the predicted interface elevations ξ for turbidity currents driven by 9, 30 and 65 μm respectively, and the Figures 5c, 6c and 7c illustrate how the corresponding

densimetric Froude numbers Fr_d vary along the model canyon and fan. The weakly depositional 9-μm turbidity currents were both predicted and observed to reach the end of the model fan at x = 11.6 m. They were supercritical along the canyon, and subcritical on the fan, with a distinct intervening hydraulic jump from supercritical flow ($Fr_d > 1$) to subcritical flow ($Fr_d < 1$), as shown in Figures 5b,c.

The underflows driven by 30 μm sediment show a tendency to drop the majority of their suspended load close to the inlet (Figure 6a). They were predicted to be dense enough to reach the model fan, while continuously decelerating and thickening after the slope break (Figure 6b). The plot of densimetric Froude number given in Figure 6c, however indicates that they reached the downstream invert at the end of the flume at x = 11.6 m without going through an internal hydraulic jump .

Numerical simulations indicated that the very strongly depositional turbidity currents generated by 65 μm sediment (Figure 7a) were unable to preserve their identity. That is, the predicted layer-averaged concentration of suspended sediment was predicted to drop below 0.1 % of the inlet value before the flow reached the end of the flume. The numerical calculations indicated that this condition was reached at x = 5.38 m for run GLASSB1, x = 5.37 m for run GLASSB2 and x = 5.95 m for run GLASSB3. The densimetric Froude number of each of these flows was predicted to increase continuously in the streamwise direction, (Figure 7c), so that no hydraulic jump was manifested (Figure 7b).

3.3 Implications of the test of the numerical model

The above test of the numerical model revealed several features worth emphasizing. Garcia (1993) specifically notes that the experiments with 4 μm and 9 μm sediment displayed hydraulic jumps, whereas those with 30 μm and 65 μm did not. In addition, he suggests that the currents with 65 μm sediment did not reach the end of the flume. The present numerical model produces results that agree with all of these observations, and is able to predict the evolution of the flow whether or not it goes through a hydraulic jump. It should be noted that Choi & Garcia (1995) also did not obtain a hydraulic jump in their numerical model of the experiments of Garcia (1993) with the 30 μm material.

In order to interpret the results, consider a turbidity current driven by appropriately fine sediment that undergoes a hydraulic jump near a slope break. Both the experiments of GGGP and the present model predict that with all other factors equal, as grain sizes coarsens the strength of the jump should weaken, until with sufficiently coarse sediment the flow traverses the slope

break with no jump whatsoever, the flow becoming ever more depositional and supercritical as it propagates downstream.

Finally, a comparison of the experimental and numerical results for run DAPER7 provide the first hint that hydraulic jumps may leave a detectable depositional signature in terms of a downstream increase in bed elevation.

4. **Numerical study of hydraulic jumps near slope breaks at experimental scale**

4.1. Some useful dimensionless parameters

Having found that the numerical model can reproduce the salient features of the internal hydraulic jumps of GGGP, the model can now be extended to a parametric study of hydraulic jumps. It is shown below that slope breaks can under the right circumstances produce both well-defined hydraulic jumps and clear depositional signatures. In this section simulations are conducted at a scale similar to that of the experiments of GGGP; an extension to field scale is discussed in a subsequent section. In addition to the densimetric Froude number Fr_d and associated bulk Richardson number Ri which were previously introduced, several dimensionless parameters introduced below are useful in characterizing the results of the numerical simulations.

Turbidity currents are non-conservative density underflows because the agent of the density difference, sediment, may be eroded into or deposited from the current. Density underflows that receive their density difference from e.g. dissolved salt are, on the other hand, conservative. Such currents can attain an equilibrium, or normal flow on a constant slope with the normal densimetric Froude number Fr_{dn} given by the relation (Ellison & Turner, 1959)

$$Fr_{dn} = \frac{S}{c_f} \tag{30a}$$

Here S denotes the bed slope and c_f is given as

$$c_f = c_D + e_w\left(2 - \frac{1}{2}Ri\right) \tag{30b}$$

Even though turbidity currents do not achieve the equilibrium of conservative density underflows, (30a) proves useful in analyzing the numerical results.

The Shields number is a dimensionless bed shear stress that characterizes the degree to which the flow can mobilize the bed sediment. It is defined as

$$\tau^* = \frac{u_*^2}{gRD} \tag{31a}$$

(31a) can be rearranged with the use of (8b) to yield the form

$$\tau^* = \left(\frac{u_*}{v_S} R_f \right)^2 \tag{31b}$$

The incremental change $\Delta\tau^*$ in Shields number associated with the change Δu_* can be similarly defined as

$$\Delta\tau^* = \left(\frac{\Delta u_*}{v_S} R_f \right)^2 \tag{31c}$$

Here $\Delta\tau^*$ denotes the drop in Shields number calculated as a difference between the average Shields number in the supercritical region just upstream of a hydraulic jump and that in the subcritical region immediately downstream, and Δu_* denotes the corresponding drop in shear velocity. This formulation is employed to analyze the relation between the drop in Shields number across a jump and the associated depositional signature.

4.2. Numerical simulations

Several scenarios for turbidity currents developing along a sloping bed were simulated numerically in order to analyze at experimental scale the effect of dimensionless parameters in (17b) on the formation of an internal hydraulic jump and a corresponding depositional signature. All calculations at experimental scale were performed using the "three-equation" model for flow dynamics and suspended sediment. With a single exception reported at the end of this section, the modeled 1D canyon-fan system had a structure identical to that of the experiments reported in GGGP; i.e an upstream "canyon" region with a length of 5 m and an initial slope $S_i \geq 0$, followed by a horizontal downstream "fan" region with a length of 6.6 m.

4.2.1. Effect of the slope break on the depositional signature

It is value to note here that the experiments reported in GGGP involve a relatively steep submarine canyon followed by a horizontal abyssal plain. The presence of a slope break was to ensure the occurrence of hydraulic jumps within the experimental domain. Also, the position of internal hydraulic jumps in turbidity currents driven by 4 and 9 μm sediment happened to loosely coincide with the position of the slope break. Therefore, any depositional signature associated with the jump would be expected to appear to be at or near the location of the canyon-fan transition. The results of numerical simulations presented below will elucidate three different scenarios related to the presence of a slope break:

1. The internal hydraulic jump occurs upstream of the slope break, in which case the major depositional signature is associated with the jump, and a minor one, which is often indiscernible or absent, is associated with the slope break.

2. The internal hydraulic jump occurs downstream of the slope break, in which case the major depositional signature is associated with the break and a minor one with the jump.

3. The internal hydraulic jump develops at the location of the slope break, in which case only one depositional signature is manifested.

4.2.2. Effect of the initial slope of the model canyon

The streamwise bed slope of submarine canyons can vary from under 0.01 (Amazon Submarine Canyon; Pirmez, 1994) to at least 0.19 (Rupert Inlet; Hay, 1987a,b; see also Barnes & Normark, 1985). The slope of a submarine fan tends to be substantially less than that of its associated canyon (e.g. Amazon Submarine Fan; Pirmez, 1994). Here, the influence of the initial slope S_i of the model canyon is investigated for five different slopes, i.e.; 0, 0.04, 0.08, 0.12 and 0.26. The model input parameters are: h_0 = 3 cm, U_0 = 8.3 cm/s, C_0 = 0.003, D =15 μm, R = 1.65, water temperature $T = 26^0$, and run time = 30 min. Note that these numbers include values that fall within the range of the experiments reported in GGGP.

Figures 8a and 8b document the relation between the canyon-fan transition and the flow. A hydraulic jump is apparent for all values of initial canyon slope S_i; its position is demarcated by the point in Figure 8b where the densimetric Froude number makes the transition from a value greater than unity to a value less than unity. In the case of a vanishing canyon slope S_i a hydraulic jump forms not far downstream of the inlet. For all other values of S_i the hydraulic jump is mediated by the break in slope at x = 5 m. For the case S_i = 0.04 the hydraulic jump occurs just upstream of the slope break at x = 5 m. As S_i increases beyond 0.04, the hydraulic jump is pushed progressively farther downstream; in the case S_i = 0.26 the jump occurs about 3.5 m beyond the slope break. When the jump occurs downstream of the slope break, the flow first responds to the slope break with a gradual decline in densimetric Froude number, and then goes through a more abrupt decline in the vicinity of the hydraulic jump. It can be seen in Figures 8a and 8b that an increase in initial canyon slope S_i results in a swifter turbidity current that decelerates more slowly, pushing the hydraulic jump farther downstream.

The patterns in densimetric Froude number evident in Figure 8b are mirrored in terms of the patterns of variation in the Shields number of Figure 8c. The Shields number drops abruptly due to the hydraulic jump when it occurs upstream of the slope break. When the hydraulic jump

occurs downstream of the slope break, the Shields number first drops gradually in response to the slope break and then abruptly at the hydraulic jump.

The resulting deposits are documented in Figure 8d. The deposit thickness is characterized in grams/cm^2; at a porosity of 0.5, 1 gram/cm^2 corresponds to a deposit thickness of 0.755 cm. Several notations have been included in order to clarify the features of Figure 8d. A vertical line has been inserted at the point of the slope break (x = 5 m). The position of the point within each hydraulic jump where Fr_d = 1 is denoted with an arrow. Finally, the two nodes demarcating an abrupt downstream change in bed elevation near the hydraulic jump are denoted with an ellipse.

In the case S_i = 0 a depositional signal is manifested in terms of an abrupt decrease in bed slope at the location of the jump (ellipse). No depositional signal is evident at x = 5 m because there is no slope break there. In all other cases a slope break is present at x = 5 m, and a depositional signal can be discerned in its vicinity in terms of a zone where bed elevation increases sharply in the downstream direction (ellipses). That is, the depositional signal takes the form of a backward-facing step.

The depositional signal is weakest for the smallest finite initial upstream slope S_i of 0.04 and is strongest for the largest value S_i = 0.26. At S_i = 0.04 the hydraulic jump begins just upstream of the slope break (Figure 9b) and the depositional signal occurs just upstream of it as well (ellipse). As S_i increases above this value the hydraulic jump is pushed farther downstream, and the signal devolves into two parts. The first part is a relatively diffuse, high-amplitude backward-facing step associated with the slope break itself, and the second part is a relatively sharp, low-amplitude backward-facing step (ellipse) associated with the resulting hydraulic jump (arrow), which is in turn driven by the slope break.

It is thus seen from Figure 8d that an abrupt slope break can leave two depositional signals; a) a relatively diffuse backward-facing step associated with flow deceleration downstream of the slope change, and b) a more abrupt backward-facing step associated with the hydraulic jump. Both signals are ultimately driven by the slope break. When the momentum of the flow is insufficient to maintain supercritical flow over a bed of vanishing slope, the two signals merge into one. When the momentum of the flow is sufficient to drive it well into the region of vanishing bed slope before the hydraulic jump occurs, the signals become distinct. All other factors being equal, an increased upstream bed slope leads to increased penetration of the supercritical flow into the zone of vanishing bed slope before the hydraulic jump occurs.

Table 2a documents the average Shields stress τ^* in the supercritical region upstream of the jump, the average Shields stress τ^* in the subcritical region downstream of the jump, and the

difference $\Delta\tau^*$ between the two. Evidently higher initial upstream slope S_i drives a higher value of $\Delta\tau^*$, and thus a stronger pair of depositional signals.

Figure 8e shows the pattern of entrainment of ambient water by the turbidity currents. In all cases simulated therein a development zone is apparent for about the first meter. Downstream of this zone, e_w is seen to be relatively large in the zone of supercritical flow, increasing in S_i. In the zone of subcritical flow farther downstream e_w drops to a very small value; the results from all numerical experiments eventually collapse onto the same curve.

4.2.3. Effect of the coefficient of bed resistance

Here the conditions of Run DAPER4 of GGGP (Table 1) are simulated for a range of bed friction coefficients, that is $0.01 \leq c_D \leq 0.05$. Note that the lower limit of 0.01 was used above for the simulation of experiments reported in GGGP. The temperature is taken to be 26^0, and the total run time is 40 min. The initial upstream bed slope S_i is that of Garcia (1989), i.e. 0.08. The downstream variation in interfacial elevation ξ is given in Figure 9a; the corresponding downstream variations in Shields stress and deposit mass per unit area are given in Figures 9b and 9c, respectively.

For $c_D = 0.01$ a hydraulic jump forms close to the canyon-fan break (Figure 9a). As the bed resistance increases, the turbidity current decelerates more rapidly due to the higher bed shear stress. As a result the internal hydraulic jump forms progressively farther upstream (Figures 9a, b). The two depositional signals of the slope break and the hydraulic jump merge into a single signal for each case, as shown in Figure 9c. While the depositional signal is clear seen for all three values of c_D, it is largest for the largest value of c_D. This is because an increased value of c_D acts to increase the Shields stress difference $\Delta\tau^*$ across the jump (Table 2). This increase does not directly affect the rate of sediment deposition, but it does cause a strong decrease in the rate of sediment erosion from the bed. This decrease is thus the ultimate cause of the depositional signal.

4.2.4. Effect of the inflow Richardson number and concentration of suspended sediment

The conditions of Run DAPER1 are simulated for a range of values of inflow volumetric concentration of suspended sediment, that is $0.0007 \leq C_o \leq 0.014$.. The lower limit of concentration corresponds to a very dilute underflows with an inflow Richardson number Ri_0 of about 0.05 ($Fr_{do} = 4.47$)), and the upper limit was determined so as to obtain an inflow Richardson number close to the unity ($Fr_{do} \cong 1$). The actual value of C_o for Run DAPER 1 was 0.00143 (Table 2). The initial upstream bed slope S_i is that of Garcia (1989), i.e. 0.08. The

results are presented in terms of profiles of bed elevation ξ in Figure 10a, flow velocity U in Figure 10b, Froude number Fr in Figure 10c, concentration C in Figure 10d and deposit mass per unit area in Figure 10e.

The turbidity currents with lower values of C_o (Ri_o) (and thus lower ratios of upstream gravitational force to inertial force) are slower and thicker in both their super- and subcritical regions (Figure 10a,b). A low value of Ri_o corresponds to a relatively high upstream inertial force, and as a result there is a tendency for the hydraulic jump to move modestly downstream as Ri_o is decreased (Figures 10a,b,c). This notwithstanding, it is seen in Figure 10c that the hydraulic jumps are all localized very near the slope break. Figure 10c also shows that the densimetric Froude number in the supercritical region quickly adopts a quasi-equilibrium value Fr_{dn} (Ellison & Turner, 1959), independently of whether the current initially accelerates or decelerates along the model canyon. Figure 10d indicates that the concentration C tends to decrease roughly exponentially in the zone upstream of the hydraulic jump, and roughly linearly in the zone downstream of the jump, with no discontinuity manifested either at the slope break or the jump.

Figure 10e shows that the strength of the depositional signals of the slope break/hydraulic jump, which are essentially consonant in these simulations. The strength of the signal clearly increases with increasing C_o (Ri_o). The case with the higest initial concentration (C_o = 0.014) shows the highest deposition rate just downstream of the outlet as well as just downstream of the hydraulic jump. This same case also shows the lowest deposition rate just upstream of the hydraulic jump. Evidently just upstream of the hydraulic jump the flow had developed to the point that erosion was almost able to balance deposition, leaving only a very thin bed deposit there.

In the above simulations, inflow Richardson number has been increased by increasing C_o and holding other parameters constant. It can be also increased by increasing the current inflow depth or decreasing the inflow depth-averaged velocity, cases which are not analyzed here.

4.2.5. Effect of the fall velocity of the median size D of the sediment

The dimensionless ratio v_s/U_o has a major influence on the cut-off size of sediment that cause a turbidity current to undergo an internal hydraulic jump. In order to study the role of this parameter, numerical experiments were performed with four sediment sizes, i.e. D = 9, 15, 20 and 30 μm. The other model input parameters are: h_0 = 3 cm, U_0 = 8.3 cm/s, C_0 = 0.003, R = 1.65, T = 26°, S_i = 0.08, run time = 40 min. The values of v_S/U_0 corresponding to the above sediment sizes are $0.88 \cdot 10^{-3}$, $2.67 \cdot 10^{-3}$, $4.90 \cdot 10^{-3}$ and $10.12 \cdot 10^{-3}$, respectively. Results are

presented in terms of the interfacial elevation ξ in Figure 11a, the densimetric Froude number Fr_d in Figure 11b and the mass sediment deposit per unit bed area in Figure 11c.

Figures 11a and 11b illustrate that the strength of the jump declines and its position is gradually pushed downstream of the slope break as D (and thus v_s) is increased. In the case of 30 μm material, the jump is extremely weak and barely occurs within the computational domain. The depositional signal is weak in all cases of Figure 11c, but is nevertheless most evident therein for the finest size studied. In aggregate the figures confirm the conclusions reached in regard to Figures 4 – 7; turbidity currents carrying sufficiently coarse material deposit sediment so rapidly that they undergo only very weak jumps if at all in response to abrupt slope breaks.

Figure 11a suggests a dimensionless criterion for the formation of a clear hydraulic jump at a slope break. In light of the fact that the cases with values of $v_s/U_o \leq 2.67 \cdot 10^{-3}$ exhibited clear hydraulic jumps and the cases with value of $v_s/U_o \geq 4.90 \cdot 10^{-3}$ did not, an appropriate approximate threshold for a clear hydraulic jump appears to be a value of v_s/U_o near $3 \cdot 10^{-3}$.

4.2.6. Effect of the multiplicative constant r_0

The constant r_o is equal to the ratio of near-bottom sediment concentration to layer-averaged sediment concentration C. In principle this parameter is a dependent variable, but in the simple layer-averaged analysis pursued here it is treated as a prescribed constant. This notwithstanding, it is expected that $r_o \geq 1$, and that $r_o \rightarrow 1$ as $u_*/v_s \rightarrow \infty$. In so far as the experiments of GGGP could be modeled well with values of r_o of 1 (4, 9 and 30 μm material) and 2 (65 μm material), the effect of varying r_o from 1 to 2 is studied here. The other model input parameters are: $h_0 = 3$ cm, $U_0 = 8.3$ cm/s, $C_0 = 0.003$, $D = 15$ μm, $R = 1.65$, $T = 26^0$, $S_i = 0.08$ and run time = 30 min. Figures 12a,b,c show profiles for ξ, Fr_d and deposit mass per unit area, respectively.

The figures illustrate the following effect of increasing r_o from 1 to 2: the hydraulic jump is pushed farther downstream of the slope break (Figures 12a,b); the net deposition rate of sediment increases and the depositional signature, already weak for the case $r_o = 1$, becomes indiscernible.

4.2.7. Effect of the sediment entrainment rate e_s

It was noted earlier that even if the flow is net depositional, erosion must be accounted for if any depositional signal of a slope break and its associated hydraulic jump is to appear. This conclusion is demonstrated more precisely in Figure 13. The figure shows the results of three paired simulations associated with 4 μm, 9 μm and 15 μm material. In one simulation of each pair the sediment entrainment rate e_s has been computed in accordance with (10), and in the other

the sediment entrainment rate has been set equal to zero, rendering the flows purely depositional. The other parameters of the simulations are h_0 = 3 cm, U_0 = 8.3 cm/s, C_0 = 0.009, R = 1.65, T = 26^0, S_i = 0.08, run time = 30 min.

It is seen from Figure 13 that no depositional signal of the slope break/jump appears if erosion is neglected. In the case of the simulations with the 9 μm and 15 μm material, the flow is net depositional everywhere even when sediment erosion is included. The deposition rate is hardly altered by the inclusion of sediment entrainment in the zone of subcritical flow downstream of the jump, but is suppressed upstream of it. This suppression allows the manifestation of the depositional signal.

In the case of the 4 μm material, the flow becomes net erosional in most of the reach upstream of the slope break. This result is consistent with possibility that such flows can under the right circumstances excavate submarine canyons. As in the other two cases, the flow is net depositional downstream of the slope break, and the deposition rate is hardly altered by the inclusion of sediment erosion.

4.2.8. Effect of the downstream boundary condition

The simulations reported above are based on the experimental configuration of Garcia (1989), in which there is an invert located at x = 11.6 m where the turbidity current flows into a damping tank. The presence of this invert results a quasi-steady turbidity current that attains a densimetric Froude number of unity at the invert. This condition has been used as the downstream boundary condition for the quasi-steady simulations reported above.

It is useful to make a comparison between flows satisfying the above boundary condition and flows that are otherwise identical but allowed to propagate freely until they die out. Such a comparison is given in Figure 14 using 4 μm, 9 μm and 15 μm material. The other parameters are: h_0 = 3 cm, U_0 = 8.3 cm/s, C_0 = 0.0086, R=1.65, T = 26^0, S_i = 0.08, run time = 40 min.

The general tendency is as follows; a) the free overfall suppresses the thickness of the turbidity current downstream of the hydraulic jump and b) the location of the jump is shifted upstream in the absence of a free overfall. The differences are least for the coarsest sediment.

It can be seen in Figure 14 that the calculation for the 4 μm material has been terminated before the current has reached the end of the plotted zone extending from x = 0 to x = 15 m. This is because the relation between the near-bed suspended sediment concentration and layer-averaged suspended sediment concentration breaks down beyond x = 11.89 m. This result highlights the desirability of extending the model to allow for values of r_o that change with changing flow conditions.

4.2.9. A hydraulic jump mediated by a gradual rather than abrupt slope break

All calculations reported above pertain to the case for which the initial bed slope S_i is a positive, constant value upstream of the point x = 5 m, and is vanishing downstream of that point. In the field, however, the transition from canyon to fan is accompanied by a gradual rather than abrupt decrease in bed slope (e.g. Figure 1). It is therefore of value to report on a calculation at the same experimental scale as those reported above, but with a gradually decreasing initial bed slope.

The calculation was performed with the conditions of run DAPER4 (Table 1), but with a modified initial profile. The modified initial bed profile consisted of an upstream zone with a constant slope of 0.0806 and a downstream zone with a constant slope of 0.0020, connected by an intermediate parabolic zone where slope changed smoothly between the two. The values of r_o and c_D used in the simulation were 1 and 0.01, respectively. Figure 15a shows the computed profiles for initial bed elevation, final elevation ξ of the interface and densimetric Froude number Fr_d. Figure 15b shows the computed profiles for the Shields stress τ^* and the mass per unit bed volume of bed deposit.

It is seen from Figure 15 that a) the decreasing bed slope results in a hydraulic jump, and b) the hydraulic jump has an easily discernible depositional signal. It follows that an abrupt slope break is necessary neither for a hydraulic jump nor for a concomitant depositional signal. As a result, the use of an abrupt slope break for most of the calculations herein should be viewed as a convenience rather than a necessity for the creation of a hydraulic jump and its depositional signal.

5. **Numerical simulations at field scale**

5.1 Simulations with the "three-equation" formulation

The results in Section 4.2.5 suggest that the parameter v_s/U_o should be less than a value of about $3 \cdot 10^{-3}$ in order for a clear hydraulic jump to form near a slope break. At the scale of the experiments of Garcia (1989), this translates into an upper bound on grain size of about 15 μm. Under appropriate circumstances, field-scale turbidity currents can be expected to attain velocities that are one to two orders of magnitude higher than those observed in the experiments of Garcia (1989). As a result, it can be expected that clear hydraulic jumps, as well as associated depositional signals would be manifested at a slope break by turbidity currents carrying material that is significantly coarser than 15 μm.

The same numerical model that has been applied above at the scale of the experiments of GGGP is equally applicable at field scale. Here such an application is carried out using the

numbers that are loosely based on inferences from the Amazon Submarine Canyon (Pirmez, 1994; Pirmez & Imran, 2003). The length of the 1D "canyon" is 2.5 km; it has a slope S_i of 0.01. The length of the 1D "fan" is 2 km; it has a vanishing slope. The sediment size was chosen to be 100 μm, i.e. fine sand, to depict the upper limit on the formation of internal hydraulic jumps at field scale. Other parameters are: h_0 = 20 m, U_0 = 3.5 m/s, C_0 = 0.01, R =1.65, Ri_o = 0.264, T = 20°, c_D = 0.05, r_o = 2, λ = 0.5, run time = 20 days. The flow was allowed to propagate freely out of the downstream end of the computational domain. A relatively high value of bed friction coefficient c_D was selected because with all other parameters unchanged smaller value of c_D led to profiles that were increasingly net erosional.

It should be noted that 20 days of continuous flow may be rather unlikely in nature. This 20 days should thus be interpreted as the sum of many sustained events, each lasting hours or perhaps a few days.

The model was changed in two ways in order to allow it to better correspond to field conditions. Firstly, the sediment entrainment formulation of Garcia & Parker (1991, 1993; Eqs. 10a-c) was replaced with that of Wright & Parker (in press; Eqs. 11a-c). Secondly, the parameter p in Eq. (11a), which controls the erodibility of the bed, was set to values less than unity, in order to characterize the likely field condition that the bed sediment has had a chance to develop some strength against erosion between turbidity current events. In particular, trial simulations performed with p = 1 (freely erodible substrate) typically led to a regime that was sufficiently erosive that the slope break in the initial condition was quickly obliterated. This result was obtained for the case p = 1 using both the "three-equation" and "four-equation" formulations. The lower value of p used in the simulation reported below insures that a net depositional (but not completely deposition) regime is attained before the slope break.

The results of the simulations are shown in Figures 16a-d. Figure 16a shows the deposit thickness attained after 20 days for the cases p = 0.007, 0.01, 0.03 and 0.06. For the case p = 0.007, a backward-facing elevation step with a height of 5.07 m extends over a length of 90 m, starting from a point 250 m downstream of the slope break. For the case p = 0.01 a step with a height of 9.28 m extends over a length of 180 m, again starting from a point 250 m downstream of the slope break. For the case p = 0.03 the step has a height of 21.95 m and extends over a length of 370 m starting 300 m upstream of the slope break. The step for the case p = 0.03 is illustrated more clearly in an inset in Figure 16a. These numbers indicate that the slope break induces a depositional signature. That this signature is also associated with a hydraulic jump is demonstrated below.

The case $p = 0.06$ is of some interest. In this case, by the end of the run the bed has undergone net erosion over a reach with a length of 530 meters, the downstream end of which is 1630 m upstream of the slope break. So much bed erosion so close to the slope break results in a bed profile near the break that increases so gently downstream that it is too diffuse to be identified as a clear step, or depositional signature. Increasing the value of p causes the erosional zone to become deeper and extend farther downstream.

Figures 16b, 16c and 16d are restricted to the cases $p = 0.01$ and $p = 0.03$. Figure 16b shows the bed and interface profiles at the end of the run; Figure 16c shows the profiles for densimetric Froude number and Shields stress, and Figure 16d shows the profiles for velocity and concentration. The plots clearly show the hydraulic jump and the resultant step deceleration of the flow. The slope break, hydraulic jump and backward-facing bed step are all seen to be positioned very close to each other. The continuity of sediment concentration across the jump is verified in Figure 16d.

Similar simulations at field scale using 20 μm sediment yield much more pronounced depositional signal, as outlined in Kostic & Parker (2004). The results are consistent with the findings of Section 4.2.5 according to which a hydraulic jump and its associated depositional signal become weaker as they approach to the threshold on the formation of internal hydraulic jumps.

5.2 Simulations with the "four equation" formulation: cyclic steps

Trial field-scale simulations were performed with the "four equation" model of turbidity current dynamics. These were run at conditions analogous to those of the previous section, and they led to very similar results: a hydraulic jump and a backward-facing step in response to the slope break. Runs yielding these results are not discussed further here. In some cases, however, the results were sufficiently different to warrant the discussion below.

An interesting feature appeared in the "high-p value" simulations with the "four equation" model that did not appear in any of the simulations with the "three equation" model; multiple upstream-migrating steps punctuated by hydraulic jumps, or "cyclic steps" (Parker & Izumi, 2000; Taki & Parker, in press, Sun & Parker, in press). An example is presented here for the case $p = 0.03$. All other parameters are the same as those of the previous section, i.e. $h_0 = 20$ m, $U_0 = 3.5$ m/s, $C_0 = 0.01$, R=1.65, $T = 20^{\circ}$, $r_o = 2$, $\lambda = 0.5$, run time = 20 days. Additional parameters required in the "four-equation" formulation are: $c_D^* = 0.005$, $\alpha = 0.1$. Figure 17 shows plots of bed and interface elevation at t = 96 hours, 192 hours, 288 hours and 480 hours

(20 days). The bed is net depositional, but the break in slope appears to trigger an instability that creates multiple, backward-facing bed steps bounded by hydraulic jumps that migrate upstream.

These trains of steps have been observed and explained in the subaerial setting (i.e. in rivers and related open channel flows with erodible beds). For example, Wohl & Grodek (1994) and Duckson & Duckson (1995) have observed rhythmic steps in the beds of bedrock streams. It is rarely possible to observe the process of incision into bedrock directly in the field. Parker & Izumi (2000), however, developed a theory to describe the formation of such steps in a purely erosional (incisional) setting. They have termed these features "cyclic steps." The theory predicts that the steps should migrate upstream and be bounded by hydraulic jumps. The only qualitative difference between bedrock steps and those shown in Figure 17 is that the in the former case the bed degrades on average due to incision, whereas in the latter case the bed is net aggradational. Brooks (2001) has modeled purely erosional cyclic steps in a model bedrock in the laboratory.

Winterwerp et al. (1992) have observed similar cyclic steps bounded by hydraulic jumps in alluvium in the field. The setting was that of sheet open channel flow over a sandy bed. Taki & Parker (in press) have called these "transportational" cyclic steps, in which bed erosion and deposition occur simultaneously. Taki & Parker (in press) and Sun & Parker (in press) have studied experimentally and modeled numerically transportational cyclic steps. One possible state is an equilibrium whereby deposition dominates on the upstream side of each step and erosion dominates on downstream side, but the train marches upstream without net bed aggradation or degradation. Similar cyclic steps bounded by hydraulic jumps can also form, however, under conditions of net bed degradation (deposition dominates erosion) or aggradation (erosion dominates deposition). This latter case provides a subaerial analog of Figure 17.

Parker & Izumi (2000) Sun & Parker (in press) have shown that cyclic steps are cousins of antidunes. In particular, under the right conditions antidunes devolve into a train of upstream-migrating steps punctuated by hydraulic jumps. Such steps are invariably long waves in that the depth (subaerial) or flow thickness (subaqueous) is small compared to step length.

The possibility of cyclic steps in the subaqueous setting has been investigated much less. Fedele & Garcia (2001) have used the "four equation" model to perform an approximate stability analysis of an erodible, sandy bed over which flows a muddy turbidity current. The analysis revealed an antidune instability. Lee et al. (2002) discuss a variety of mechanisms for the formation of submarine sediment waves, including antidunes. Included in their treatment is a numerical model of flow over a wavy bed using the turbidity current formulation of Skene et al.

(1997); the model again yields upstream-migrating antidunes. The results of Figure 17, however, provide the first hint that many upstream-migrating submarine bedforms, including those commonly found on the back side of levees bounding submarine channels, may actually be subaqueous versions of cyclic steps.

6. **Conclusions**

The analysis presented here helps define the limits on the formation of internal hydraulic jumps in turbidity currents near a canyon-fan transition. It also provides clear evidence that a hydraulic jump associated with slope decline in the downstream direction can indeed affect the resulting sediment deposit by leaving a depositional signature. When the signature occurs, it can take the form of one, or in some cases two backward-facing steps. The case of two steps occurs when the jump forms well downstream of the slope change that generates it. In such a case the gradual deceleration of the flow between the step and the jump creates a relatively gentle step, and the sudden deceleration across the jump creates a sharp step. When the jump occurs near the point at which slope changes, the two steps merge into one.

The analysis underlines the physical basis for the depositional signature of the jump. Suspended sediment concentration is continuous through a hydraulic jump, and the deposition rate of sediment is proportional to this concentration. As a result, a purely depositional formulation of the problem fails to capture any depositional signature of the jump. When sediment entrainment is included, however, a step decrease in entrainment rate is realized across the jump due to the step decrease in flow velocity and shear stress. The net depositional rate (deposition rate – entrainment rate) thus undergoes a step increase across the jump. In this way, a depositional signature in the form of a backward-facing step is realized even when erosion nowhere dominates deposition.

The numerical model used to obtain the results reported above employs the explicit finite-volume upwind ULTIMATE QUICKEST algorithm. The bed is allowed to evolve as a result of simultaneous erosion and deposition of suspended sediment. The experimental data on the downstream variation in sediment mass deposited per unit bed area (Garcia, 1993) were used to calibrate and verify the model. The model is applied to the various scenarios of turbidity currents developing along a sloping bed, designed to be representative of experiments by GGGP. The results of the model simulations using the "three equation" formulation for turbidity current dynamics lead to the following observations and conclusions:

- Turbidity currents driven by sediment fine enough to satisfy the condition $v_S / U_0 < 2.67 \cdot 10^{-3}$ regularly display an internal hydraulic jump induced by the break in

slope. The coarser-grained currents, for which the ratio $v_S/U_0 > 4.9 \cdot 10^{-3}$, do not undergo a transition to subcritical flow due to the rapid rate of sediment deposition on the bed. They either thicken after the break in slope or, if very coarse-grained, disintegrate rapidly before even reaching the model fan; in both cases the densimetric Froude number increases rather than decreases downstream of the slope break. Turbidity currents with ratios $2.67 \cdot 10^{-3} \le v_S/U_0 \le 4.9 \cdot 10^{-3}$ can go either way, depending on other dimensionless parameters. For example, higher inflow concentration C_0, higher bed resistance c_D, or milder initial canyon slope S_i generally push the cutoff ratio toward and even somewhat beyond the upper limit.

- When a hydraulic jump occurs in response to a slope break, it need not occur precisely at the slope break. Depending on the flow conditions the jump may form upstream of the slope break, be coincident with it or occur downstream of the slope break. In the last case a gradual reduction in shear stress is manifested downstream of the slope break up to the hydraulic jump, where a sharper break occurs. In the numerical experiments at laboratory scale reported here, a progressively steeper upstream reach/model canyon (e.g. S_i > 0.12) pushes the internal hydraulic jump increasingly farther downstream of the slope break.
- Both the gradual reduction in bed shear stress between the slope break and the jump and the sharper reduction at the jump can leave depositional signals in the form of backward-facing steps. The two steps merge into a single step when the slope break and the jump are coincident.
- In the original work of Garcia (1989), it is reported that the break in slope and associated hydraulic jump did not leave a discernible signature. A reanalysis of the same data reveals at least one case with a weak signature. This signature is not reproduced by the numerical model of Choi & Garcia (1995) because it is purely depositional. It is captured reasonably well by the present model, which incorporates entrainment of bed sediment into the analysis. The analysis provides the following crude criterion for a depositional signature of the jump: $\left(\Delta u_*/v_S R_f\right)^2 > 0.3$. The precise criterion depends on other dimensionless parameters as well.
- The slope break need not be sharp in order to generate a hydraulic jump and a depositional signature.

When the analysis is extended to the "four equation" model of turbidity current dynamics, under conditions of increasing sediment entrainment the slope break can trigger an

instability which generates a series of upstream-migrating cyclic steps bounded by hydraulic jumps. These steps constitute a newly-recognized phenomenon that deserves further investigation.

Acknowledgements

This material is a contribution of the National Center for Earth-surface Dynamics. The Center is funded by the National Science Foundation STC Program under agreement number EAR-0120914.

Notation

α	constant in the sediment entrainment relation
α_1, α_2	parameters in the sediment entrainment relation
β_2	shape constant accounting for a nonuniform density over current depth
c_D	bed friction coefficient
c_f	total friction factor
c_o , c , $c\pm$	characteristic velocities of the turbid flow
C	turbidity current depth-averaged volumetric concentration
$\hat{C}$	dimensionless depth-averaged volumetric concentration
$\hat{C}_t$	target concentration
D	median diameters of sediment
e_w	water entrainment coefficient
Frd	densimetric Froude number
Frd_n	normal densimetric Froude number
Frd_p	densimetric Froude number just upstream of the plunge point
Frd_d	densimetric Froude number just downstream of the plunge point
f, f_1, g_1	functions
g	acceleration of gravity
h	turbidity current thickness
$\hat{h}$	dimensionless turbidity current thickness
h_0 , U_0 , C_0	values of h, U and C at the inflow boundary
$\hat{L}$	dimensionless target length

$\hat{q}$, $\hat{\phi}$	dimensionless conservative variables defined such that $\hat{q} = \hat{U}\hat{h}$ and $\hat{\phi} = \hat{C}\hat{h}$
R	submerged specific gravity of sediment
Ri	bulk Richardson number
Ri_0	Richardson number at the inflow boundary
R_f	dimensionless particle fall velocity
Re_p	particle Reynolds number
r_o	multiplicative constant
s	position of the front of the turbidity current
$\hat{s}$	dimensionless position of the front
$\dot{s}$	velocity of the current head
$\hat{\dot{s}}$	dimensionless $\dot{s}$
S	bed slope
S_i	initial slope of the canyon bed
t	time
T	temperature of the underflow
χ_h	scale ratio for length
χ_C	scale ratio for concentration
u_*	shear velocity
Δu_*	average drop in shear velocity due to internal hydraulic jump
U	turbidity current depth-averaged velocity
$\hat{U}$	dimensionless depth-averaged velocity
v_S	fall velocity of sediment
x	bottom-attached streamwise coordinate on lake bed
x^*	bottom-attached dimensionless streamwise coordinate
Δ	volume deposition rate of sediment per unit bed area per unit time
η	elevation of the bed
$\hat{\eta}$	dimensionless bed elevation
λ	porosity of deposit
ν	kinematic viscosity of the water
τ	dimensionless time

τ_s^* bed Shields stress

$\Delta\tau^*$ average drop in bed Shields stress associated with the hydraulic jump

Z similarity variable

REFERENCES

BADDOUR, R. E., 1987, Hydraulics of shallow and stratified mixing channel, *Journal of Hydraulic Engineering*, 113(5), 630-645.

BARNES, N. E. & NORMARK, W. E., 1985, Diagnostic parameters for comparing modern submarine fans and ancient turbidite systems, in *Submarine fans and related turbidite systems*, Bouma, Normark & Barnes (eds), , Springer-Verlag, New York, 13-14.

BOUMA, A. H., NORMARK, W. R. & BARNES, N. E., 1985, Submarine fans and related turbidite systems, *Springer – Verlag,* New York, 29-34.

BROOKS, P. C., 2001, *Experimental study of erosional cyclic steps*, M.S. Thesis, University of Minnesota, Minneapolis, Minnesota.

CHOI, S. U. & GARCIA, M., 1995, Modeling of one-dimensional turbidity currents with a dissipative – Galerkin finite element method, *Journal of Hydraulic Research*, 33, 623-647.

CRANK, J., 1984, *Free and moving boundary problems*, Clarendon Press, Oxford, 425 p.

DIETRICH, E. W., 1982, Settling velocity of natural particles, Water Resources Research, 18 (6), 1626-1982.

DUCKSON, JR., D. W. & DUCKSON, L. J., 1995, Morphology of bedrock step pool systems, *Wat. Res. Bull*. 31, 43-51.

ELLISON, T. H. & TURNER, J. S., 1959, Turbulent entrainment in stratified flows, *J. Fluid Mech.*, 6, 423-448.

ETTEMA, R., 2000, *Hydraulic Modeling Concepts and Practice*, ASCE Manual No. 97, American Society of Civil Engineers, 390 p.

FEDELE, J. J. & GARCIA, M. H., 2001, Bedforms and density underflows in the marine environment, *Proceedings* 2nd IAHR Symp. on River, Coastal and Estuarine Morphodynamics, Obihiro, Japan, September 10-14.

FUKUSHIMA, Y, PARKER, G. & PANTIN, H. M., 1985, Prediction of ignitive turbidity currents in Scripps Submarine Canyon, *Marine Geology*, 67, 55-81.

GARCIA, M., 1989, Depositing and eroding sediment-drive flows: Turbidity currents, Ph.D. Thesis, Department of Civil Engineering, University of Minnesota, Minneapolis.

GARCIA, M. & PARKER, G., 1989, Experiments on hydraulic jumps in turbidity currents near a canyon-fan transition, *Science*, 245.

GARCIA, M. & PARKER, G., 1993, Experiments on the entrainment of the sediment into suspension by a dense bottom current, *Journal of Geophysical Research*, 98, 4793-4807.

GARCIA, M., 1993, Hydraulic jumps in sediment-driven bottom currents, *Journal of Hydraulic Engineering*, 119(10), 1-24.

HAY, A.E. 1987a, Turbidity currents and submarine channel formation in Rupert Inlet, British Columbia, 1. Surge observations, *J. Geophys. Res.* 92(c3), 2875-2881.

HAY, A.E. 1987b, Turbidity currents and submarine channel formation in Rupert Inlet, British Columbia, 2. The roles of continuous and surge type, *J. Geophys. Res.* 92(c3), 2883-2900.

HIRSCH, 1990, *Numerical Computation of Internal and External Flows, Vol. 2, Computational Methods for Inviscid and Viscous Flows*. John Wiley, New York.

INMAN, D. L., NORDSTROM, C. E. & FLICK, R. E., 1976, Currents in submarine canyons: An air-sea-land interaction, *Annual Review of Fluid Mechanics*, 275-310.

KOMAR, P. D., 1971, Hydraulic jumps in turbidity currents, *Bulletin of Geological Society of America*, 82, 1477-1488.

KOSTIC, S., 2001, Modeling of progradational sand-mud deltas with plunging depositional turbidity currents, Ph.D. Thesis, Department of Civil Engineering, University of Minnesota, Minneapolis.

KOSTIC, S. & PARKER, G., 2003a, Progradational sand-mud deltas in lakes and reservoirs: Part 1. Theory and numerical modeling, *Journal of Hydraulic Research*, 41 (2), 127-140.

KOSTIC, S. & PARKER, G., 2003b, Progradational sand-mud deltas in lakes and reservoirs: Part 2. Experiment and numerical simulation, *Journal of Hydraulic Research*, 41 (2), 141-152.

KOSTIC, S. & PARKER, G., 2004, Can an internal hydraulic jump be inferred from the depositional record of a turbidity current?, *Proceedings*, River Flow 2004, 2nd International Conference on Fluvial Hydraulics, Naples, Italy, June 23-25.

LAMB, M. P.,HICKSON, T., MARR, J. G., SHEETS, B., PAOLA, C. & PARKER, G., 2004, Surging versus continuous turbidity currents: flow dynamics and deposits in an experimental intraslope minibasin, *Journal of Sedimentary Research*, 74(1).

LEE, H. J., SYVITSKI, J. P M., PARKER, G., ORANGE, D., LOCAT, J., HUTTON, E.W.H & IMRAN, J., Distinguishing sediment waves from slope failure deposits: field examples, including the ‘ Humboldt slide,and modelling results, Marine Geology 192 (2002) 79-104.

LEONARD, B.P., 1979, A stable and accurate convection modeling procedure based on quadratic upstream interpolation, *Comp. Methods in Applied Mechanics and Engineering*, 19, 59-98.

LEONARD, B.P.,1991, The ULTIMATE conservative difference scheme applied to unsteady one-dimensional advection, *Comp. Methods in Applied Mechanics and Engineering*, 88, 17-77.

MENARD, H. W., 1964, *Marine Geology of the Pacific*, McGraw-Hill, New York.

MUTTI, E., 1977, Distinctive thin-bedded turbidite facies and related depositional environments in the Eocene Hecho Group (South-central Pyrenees, Spain), *Sedimentology*, 24, 107-131.

NORMARK, W. R. & PIPER, D. J. W., 1991, Initiation processes and flow evolution of turbidity currents: Implications for the depositional record, *From Shoreline to Abyss: Contributions in Marine Geology in Honor of Francis Parker Shepard*, 46, 207-230.

PANTIN, H. M, 1979, Interaction between velocity and effective density in turbidity flow: phase-plane analysis, with criteria for autosuspension, *Marine Geology*, 31, 59-99.

PARKER, G., 1982, Conditions for the ignition of catastrophically erosive turbidity currents, *Marine Geology*, 46, 307-327.

PARKER, G., FUKUSHIMA, Y. & PANTIN, H.M.,1986, Self-accelerating turbidity currents, *Journal of Fluid Mechanics*, 171, 145-181.

PARKER, G., GARCIA, M., FUKUSHIMA, Y. & YU, W., 1987, Experiments on turbidity currents over an erodible bed, *Journal of Hydraulic Research*, 25, 123-147.

PARKER, G. & IZUMI, N., 2000, Purely erosional cyclic and solitary steps created by flow over a cohesive bed, *J. Fluid Mech*. 419, 203-238.

PIRMEZ, C., 1994, Growth of a Submarine meandering channel-levee system on Amazon Fan, Ph.D. thesis, Columbia University, New York, 587 p.

PIRMEZ, C. & IMRAN, J., 2003, Reconstruction of turbidity currents in Amazon Channel, *Marine and Petroleum Geology* 20(6-8), 823-849.

RAJARATNAM, N., TOVELL, D. & LOEWEN, M., 1988, Internal jumps in two-layer stratified flows, Technical report (WRE-88-4), Department of Civil Engineering, University of Alberta, Canada.

RUSSELL, H. A. J. & ARNOTT, R. W. C., 2003, Hydraulic-jump and hyperconcentrated-flow deposits of a glacigenic subaqueous fan: oak ridges moraine, southern Ontario, Canada, *Journal of Sedimentary Research*, 73(6), 887-905.

SKENE, K., MULDER, T. & SYVITSKI, J.P.M., 1997, INFLO1: A model predicting the behaviour of turbidity currents generated at a river mouth, *Comput. Geosci*. 23, 975-991.

STEFAN, H. & HAYAKAWA, N., 1972, Mixing induced by an internal hydraulic jump, *Water Resources Bulletin*, 8 (3), 531-545.

SUN, T. & PARKER, G., accepted, Transportational cyclic steps created by flow over an erodible bed. Part 2. Theory and numerical simulation*, J. Hydr. Res*.

TAKI, K. & PARKER, G. accepted, Transportational cyclic steps created by flow over an erodible bed. Part 1. Experiments, *J. Hydr. Res*.

TONIOLO, H., 2003, Debris flow and turbidity current deposition in the deep sea and reservoirs, Ph.D. thesis, University of Minnesota, 2002, 233 p.

VAN ANDEL, T. H. & KOMAR, P. D., 1969, Ponded sediment of the Mid-Atlantic Ridge between 22 and 23 degrees north latitude, *Bulletin of Geological Society of America*, 80, 1163-1190.

WILKINSON, D. L. & WOOD, I. R., 1971, A rapidly varied flow phenomenon in a two-layer flow, *Journal of Fluid Mechanics*, 47 (2), 241-256.

WINTERWERP, J. C., BAKKER, W. T., MASTBERGEN, D. R. & VAN ROSSUM, H. 1992, Hyperconcentrated sand-water mixture flows over erodible bed, *J. Hydr. Engrg.,* 119(11), 1508-1525.

WOHL, E. E. & GRODEK, T., 1994, Channel bed-steps along Nahal Yael, Negev desert, Israel, *Geomorphology*, 9, 117-126.

WOOD, I. R. & SIMPSON, J. E., 1984, Jumps in layered miscible fluids, *Journal of Fluid Mechanics*, 140, 329-342.

YIH, C. S. & GUHA, C. R., 1955, Hydraulic jumps in a fluid system of two layers, *Tellus*, 7 (3), 358-366.

FIGURE CAPTIONS

Figure 1 Plot of the long profile of the thalweg of the dominant channel of the Amazon Canyon-Fan System. The origin of the horizontal coordinate system is the approximate position of the break between the continental shelf and slope. Also shown on the plot are a) an elevation profile of the approximate top of canyon to the canyon-fan transition, and b) an elevation profile of the approximate top of the levee(s) bounding the channel on the fan. The plot derives from Pirmez (1994) and Pirmez and Imran (2003); the data were provided by C. Pirmez.

Figure 2 Diagram showing the configuration of the flume for the experiments of Garcia (1989).

Figure 3 Numerical simulation of Exp. NOVA1 of Garcia (1989) using 4 μm sediment.

a) Development of the interface between the turbid flow and the clear water above, showing the evolution of a hydraulic jump; and

b) spatial variation of the densimetric Froude number at various times, again showing the evolution of a hydraulic jump.

Figure 4 Verification of the model against the experimental data of Exp. NOVA2 of Garcia (1989) using 4 μm sediment; also included are the results of a numerical model by Choi & Garcia (1995).

a) Spatial variation of the elevation ξ of the interface between the turbid flow and the clear water above with distance from the inlet; and

b) Spatial variation of the depth-averaged velocity U and concentration C with distance from the inlet.

Figure 5 Predictions of the model for turbidity currents driven by 9 μm sediment (Exps. DAPER4 and DAPER7).

a) Depositional pattern predicted by the model; also included are the experimental observations of Garcia (1989);

b) Numerical simulation of the elevation ξ of the underflow interface; and

c) Numerical simulation of the densimetric Froude number Fr_d.

Figure 6 Predictions of the model for turbidity currents driven by 30 μm sediment (GLASSA1, GLASSA2, GLASSA3).

a) Depositional pattern predicted by the model; also included are the experimental observations of Garcia (1989);

b) Numerical simulation of the elevation ξ underflow interface; and

c) Numerical simulation of the densimetric Froude number Fr_d.

Figure 7 Predictions of the model for turbidity currents driven by 65μm sediment (GLASSB1, GLASSB2, GLASSB3).

a) Depositional pattern predicted by the model; also included are the experimental observations of Garcia (1989);

b) Numerical simulation of the elevation ξ of the underflow interface; and

c) Numerical simulation of the densimetric Froude number Fr_d.

Figure 8 Effect of the initial upstream slope of the submarine canyon on the turbidity current and deposit.

a) Variation of the elevation ξ of the underflow interface with distance from the inlet;

b) Variation of the densimetric Froude number Fr_d with distance from the inlet;

c) Variation in bed Shield stress τ^* with distance from the inlet;

d) Depositional patterns produced by the flows; and

e) Variation in water entrainment coefficient along the model canyon-fan.

Figure 9 Effect of the bed resistance on the turbidity current and deposit.

a) Variation of the elevation ξ of the underflow interface with distance from the inlet;

b) Variation of the bed Shields stress τ^* with distance from the inlet. along the model canyon-fan; and

c) Depositional patterns produced by the flows.

Figure 10 Effect of the inflow concentration (inflow Richardson number) on the turbidity current and deposit.

a) Variation of the elevation ξ of the underflow interface with distance from the inlet;

b) Variation of depth-averaged velocity U with distance from the inlet;

c) Variation of the densimetric Froude number Fr_d with distance from the inlet;

d) Variation of the volume sediment concentration C with distance from the inlet; and

e) Depositional patterns produced by the flows.

Figure 11 Effect of characteristic sediment size (fall velocity) on the turbidity current and deposit.

a) Variation of the elevation ξ of the underflow interface with distance from the inlet;

b) Variation of densimetric Froude number Fr_d with distance from the inlet; and

c) Depositional patterns produced by the flows.

Figure 12 Effect of the multiplicative constant r_0 on the turbidity current and deposit.

a) Variation of the elevation ξ of the underflow interface with distance from the inlet;

b) Variation of densimetric Froude number Fr_d with distance from the inlet; and

c) Depositional patterns produced by the flows.

Figure 13 Comparisons of simulated depositional patterns produced by including and neglecting sediment entrainment in the calculation.

Figure 14 Comparisons of the elevation ξ of the underflow interface predicted with a free overfall at x = 11.6 m and free runout of the current with no overfall.

Figure 15. Results for a simulation with an initial bed slope that declines smoothly in the downstream direction.

a) Downstream variation of initial bed elevation, elevation ξ of the underflow interface and densimetric Froude number Fr_d; and

b) Downstream variation of Shields stress τ^* and deposit mass per unit bed area.

Figure 16 Results of field-scale simulations for a turbidity current carrying 100 μm sediment using the "three equation model" after 20 days of continuous flow.

a) Downstream variation in deposit thickness for the cases p = 0.007, 0.01, 0.03 and 0.06;

b) Downstream variation in bed elevation η and interface elevation ξ for the cases p = 0.01 and 0.03;

c) Downstream variation in densimetric Froude number Fr_d and Shields stress τ^* for the cases p = 0.01 and 0.03; and

d) Downstream profiles for layer-averaged flow velocity U and suspended sediment concentratin C for the cases p = 0.01 and 0.03.

Figure 17 Simulated downstream profiles of bed elevation η and interface elevation ξ at four times during 20 days of continuous flow of a turbidity current carrying 100 μm sand, using the "four equation" model. In the simulation p = 0.03. The figure documents the formation of upstream-migrating cyclic steps bounded by hydraulic jumps.

Table 1. Input parameters for the numerical model (from experiments by Garcia, 1993)

Run	H (cm)	U (cm/s)	C x 10^3	R	Ri_o	D (μm)	v_s (cm/s)	T (^oC)	Run time (min)
NOVA1	3	8.3	1.30	1.65	.09163	4	.00115	25.5	40
NOVA2	3	8.3	2.48	1.65	.17481	4	.00114	25	40
DAPER1	3	8.3	1.43	1.65	.10080	9	.00731	26	40
DAPER4	3	8.3	2.95	1.65	.20494	9	.00741	26.5	33
DAPER7	3	8.3	8.6	1.65	.60620	9	.00677	23	30
GLASSA2	3	8.3	3.39	1.50	.21723	30	.08402	26	30
GLASSA5	3	8.3	3.94	1.50	.25248	30	.08402	26	30
GLASSA7	3	11.0	2.66	1.50	.09705	30	.08402	26	30
GLASSB1	3	11.0	3.00	1.50	.10945	65	.35418	25	38
GLASSB2	3	11.0	6.00	1.50	.21890	65	.34423	23.5	27
GLASSB3	3	11.0	1.50	1.50	.05473	65	.34104	23	28

Table 2. Effect of the bed resistance to the average Shield stress

c_D	Avg. τ^* supercritical region	Avg. τ^* subcritical region	$\Delta \tau^*$
0.01	0.45	0.09	0.36
0.02	0.72	0.14	0.58
0.05	1.20	0.27	0.93

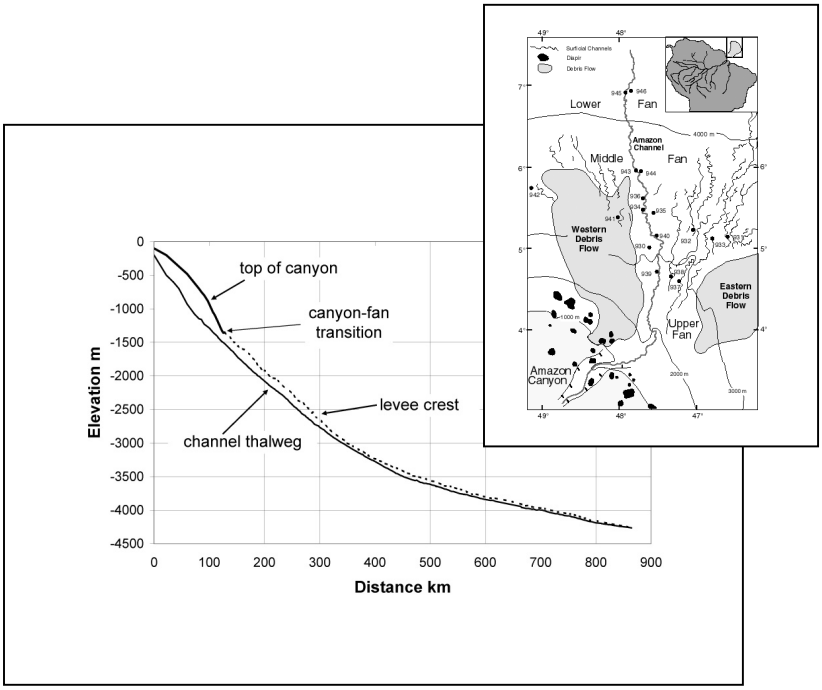

Figure 1

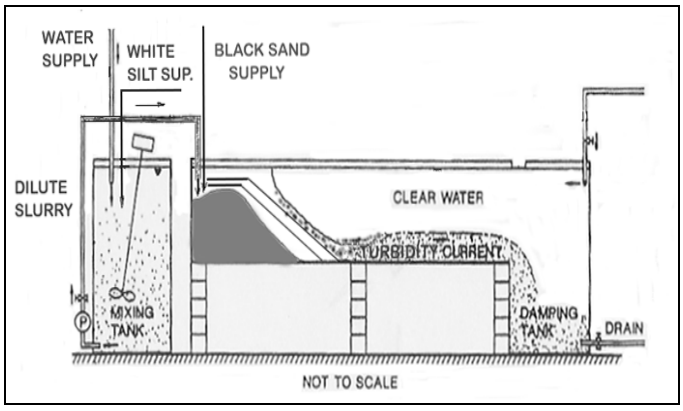

Figure 2

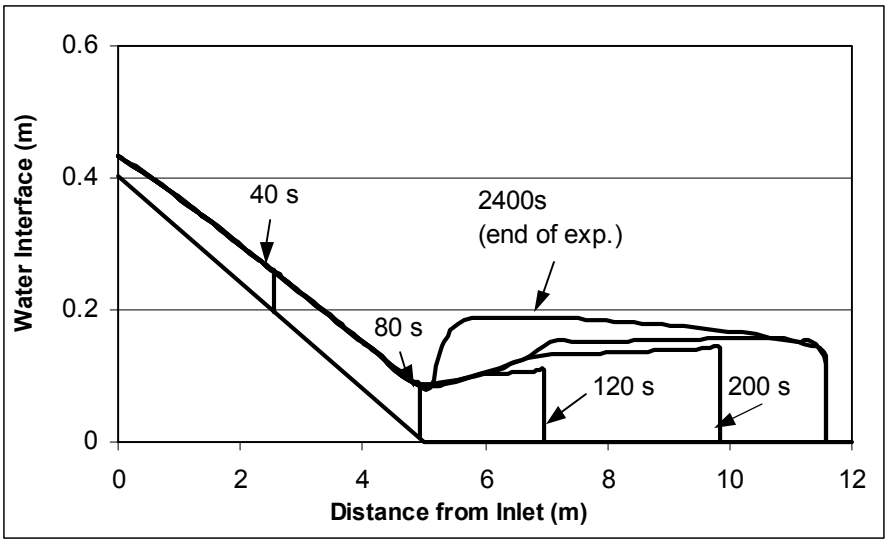
Water Interface (m)
0.6
0.4
0.2
0
40 s
2400s
(end of exp.)
80 s
120 s
200 s
0
2
4
6
8
10
12
Distance from Inlet (m)

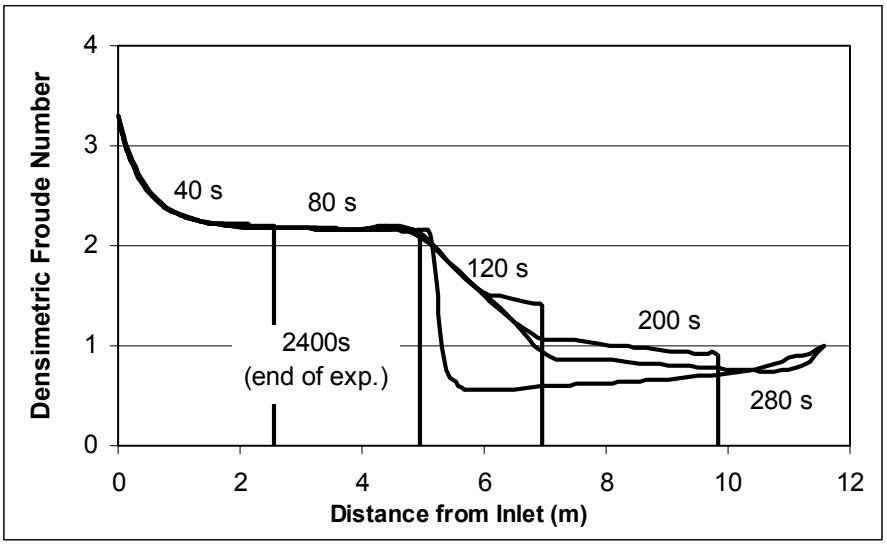
Densimetric Froude Number
4
3
2
1
0
40 s
80 s
120 s
200 s
2400s
(end of exp.)
280 s
0
2
4
6
8
10
12
Distance from Inlet (m)

Figure 3a, b

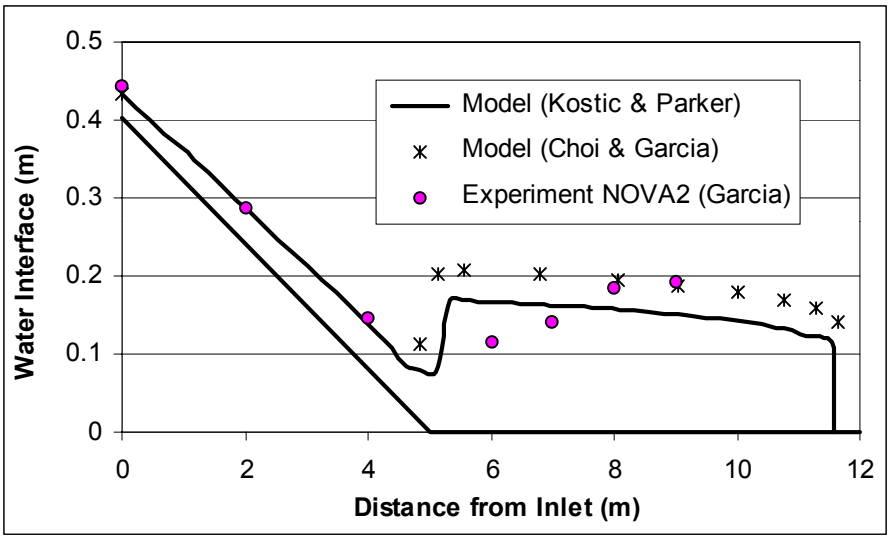
0.5
0.4
0.3
0.2
0.1
0
Water Interface (m)
0
2
4
6
8
10
12
Distance from Inlet (m)
Model (Kostic & Parker)
Model (Choi & Garcia)
Experiment NOVA2 (Garcia)

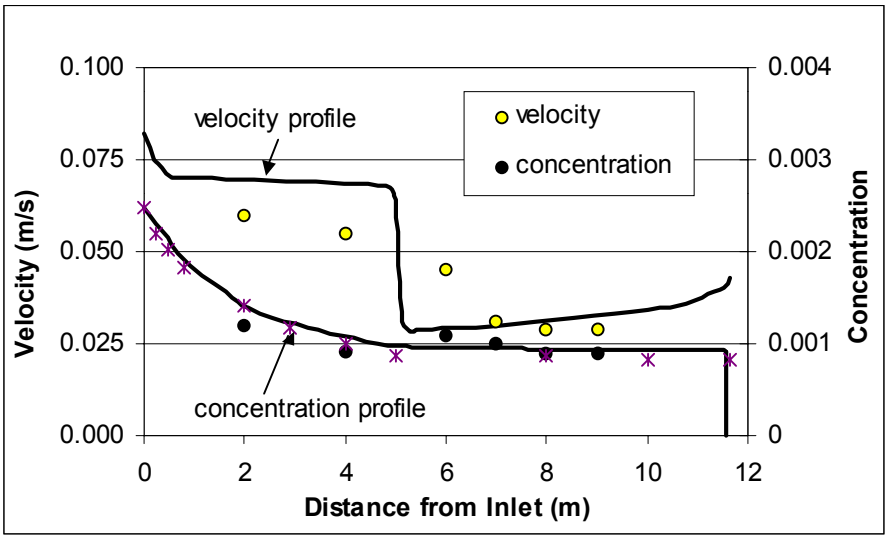
0.100
0.075
0.050
0.025
0.000
Velocity (m/s)
0.004
0.003
0.002
0.001
0
Concentration
velocity profile
concentration profile
velocity
concentration
0
2
4
6
8
10
12
Distance from Inlet (m)

Figure 4a, b

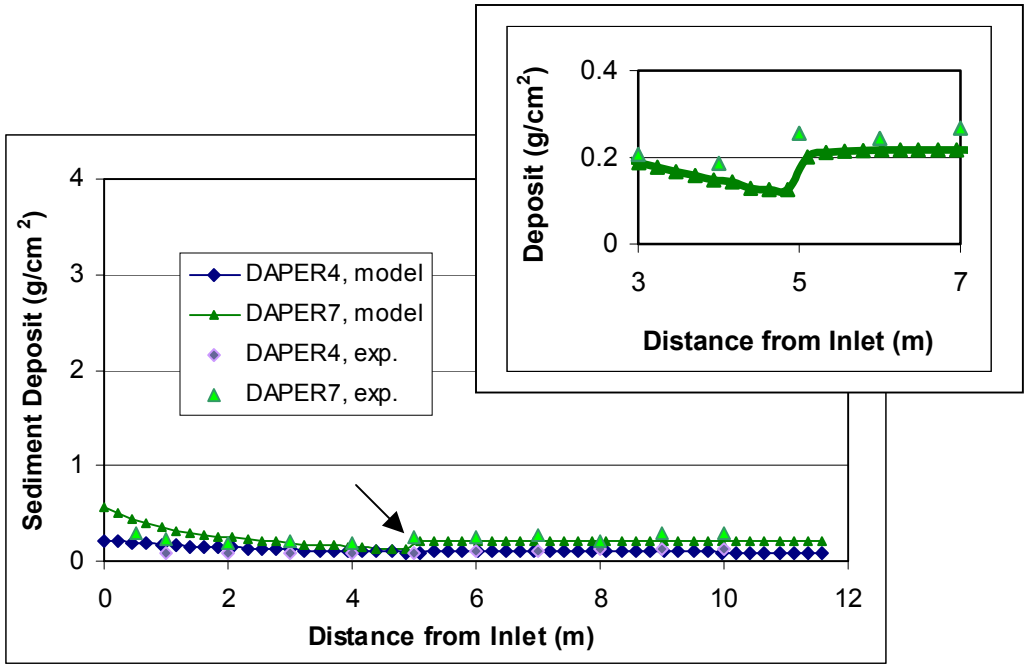
Deposit (g/cm2)
0.4
0.2
0
3
5
7
Distance from Inlet (m)

Sediment Deposit (g/cm 2)
DAPER4, model
DAPER7, model
DAPER4, exp.
DAPER7, exp.
0
1
2
3
4
0
2
4
6
8
10
12
Distance from Inlet (m)

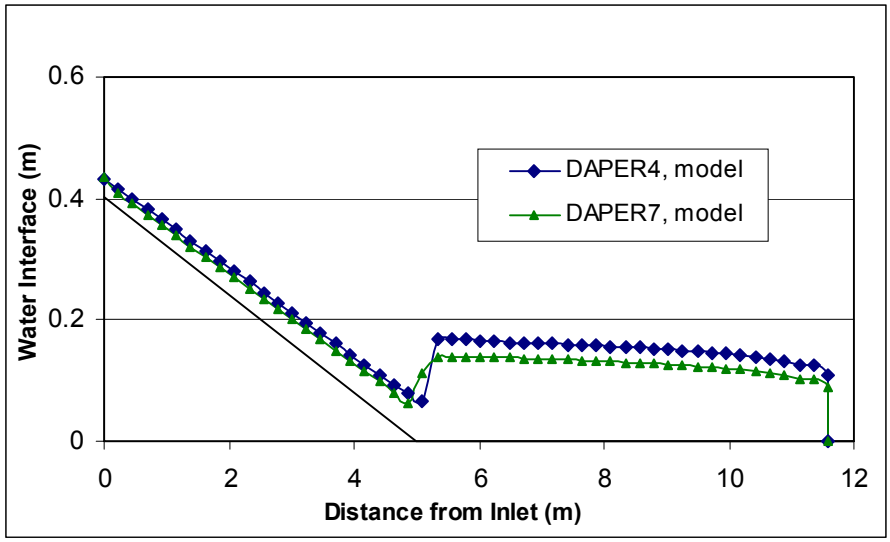
Water Interface (m)
DAPER4, model
DAPER7, model
0
0.2
0.4
0.6
0
2
4
6
8
10
12
Distance from Inlet (m)

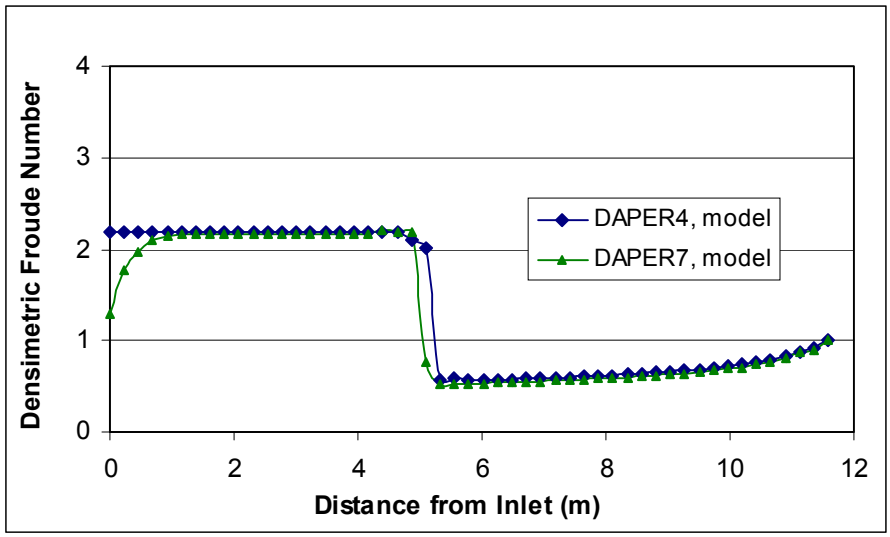
Densimetric Froude Number
DAPER4, model
DAPER7, model
0
1
2
3
4
0
2
4
6
8
10
12
Distance from Inlet (m)

Figure 5a, b, c

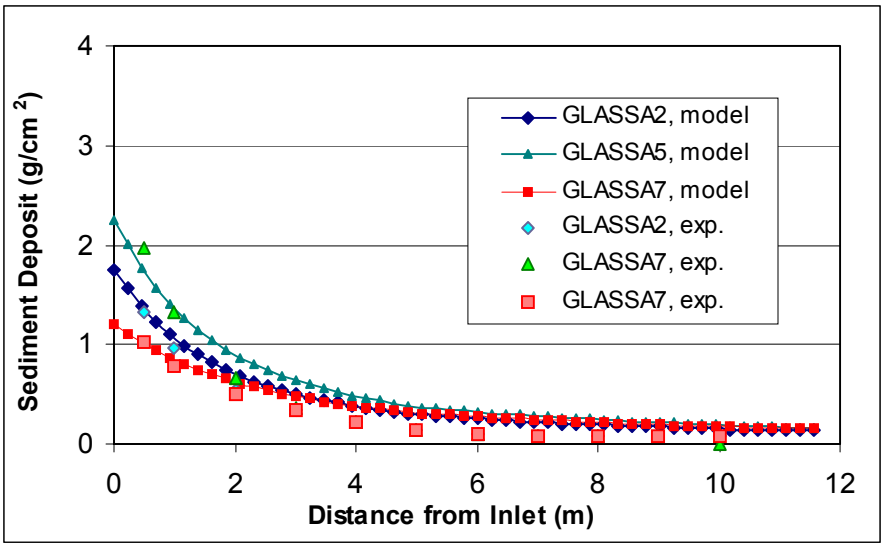
Sediment Deposit (g/cm 2)
Distance from Inlet (m)
GLASSA2, model
GLASSA5, model
GLASSA7, model
GLASSA2, exp.
GLASSA7, exp.
GLASSA7, exp.

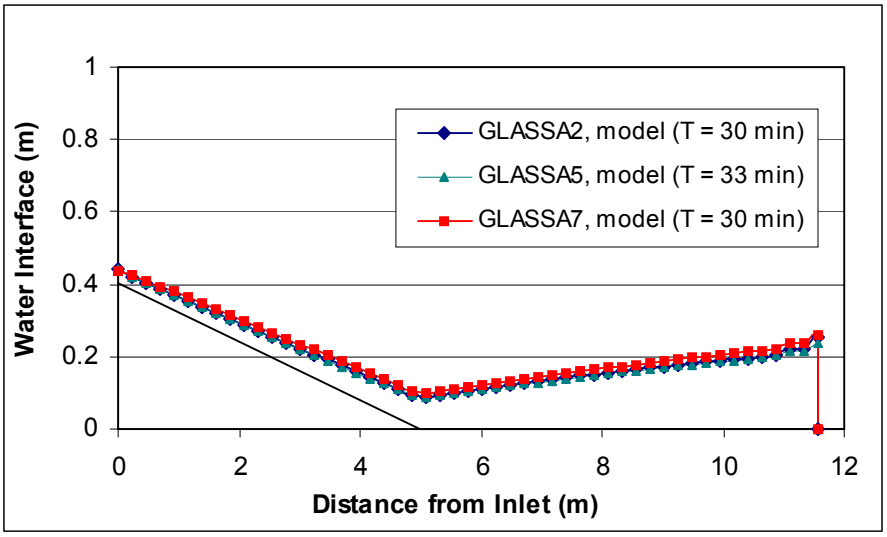
Water Interface (m)
Distance from Inlet (m)
GLASSA2, model (T = 30 min)
GLASSA5, model (T = 33 min)
GLASSA7, model (T = 30 min)

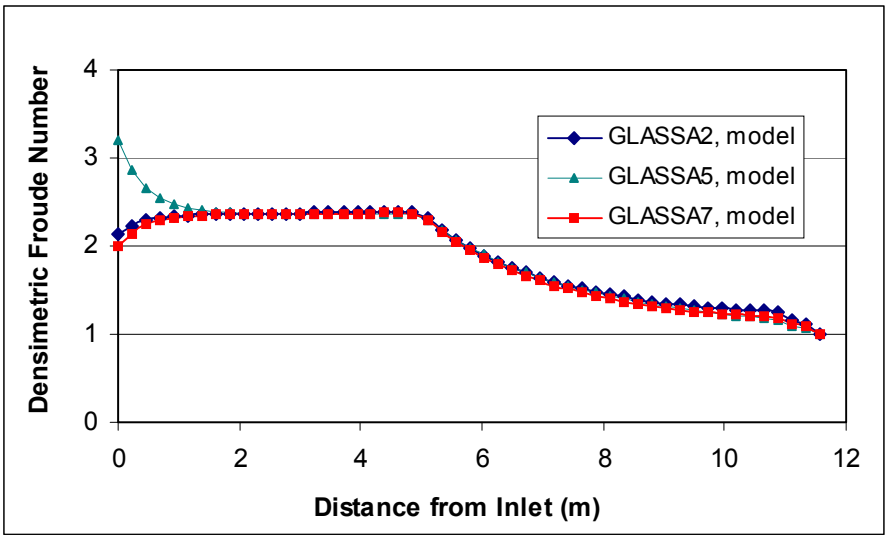
Densimetric Froude Number
Distance from Inlet (m)
GLASSA2, model
GLASSA5, model
GLASSA7, model

Figure 6a, b, c

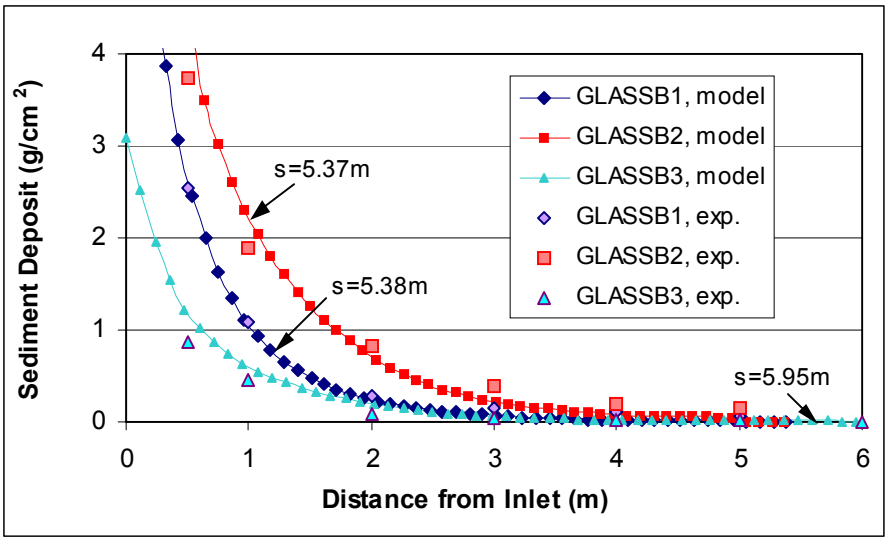
Sediment Deposit (g/cm 2)
Distance from Inlet (m)
GLASSB1, model
GLASSB2, model
GLASSB3, model
GLASSB1, exp.
GLASSB2, exp.
GLASSB3, exp.
s=5.37m
s=5.38m
s=5.95m

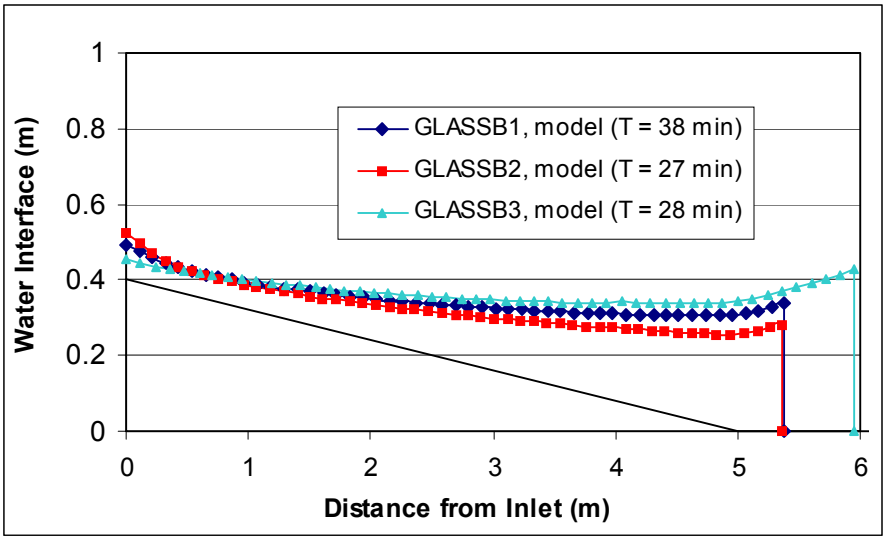
Water Interface (m)
Distance from Inlet (m)
GLASSB1, model (T = 38 min)
GLASSB2, model (T = 27 min)
GLASSB3, model (T = 28 min)

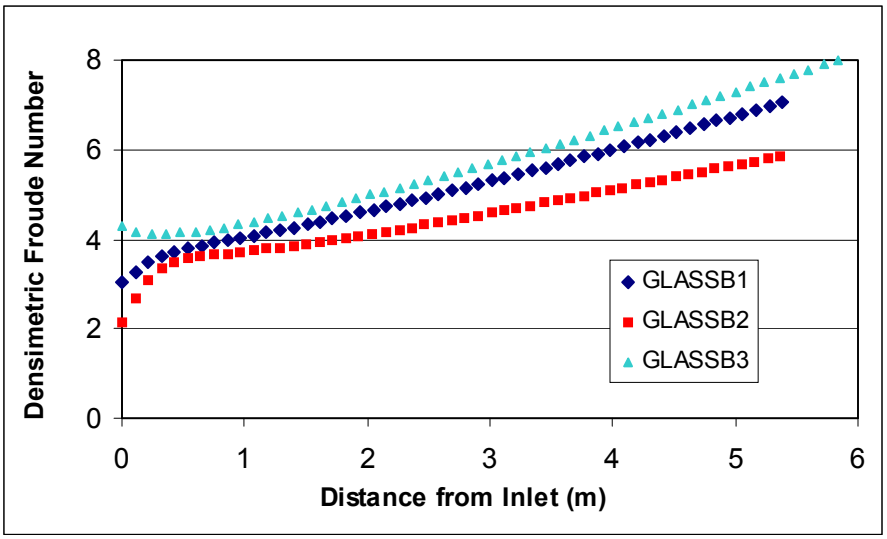
Densimetric Froude Number
Distance from Inlet (m)
GLASSB1
GLASSB2
GLASSB3

Figure 7a, b, c

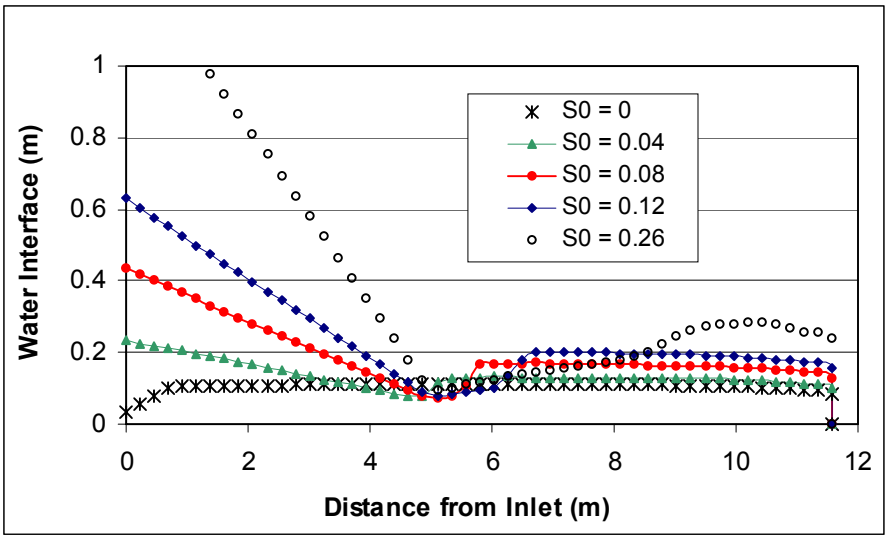
Water Interface (m)
Distance from Inlet (m)
S0 = 0
S0 = 0.04
S0 = 0.08
S0 = 0.12
S0 = 0.26
0
0.2
0.4
0.6
0.8
1
0
2
4
6
8
10
12

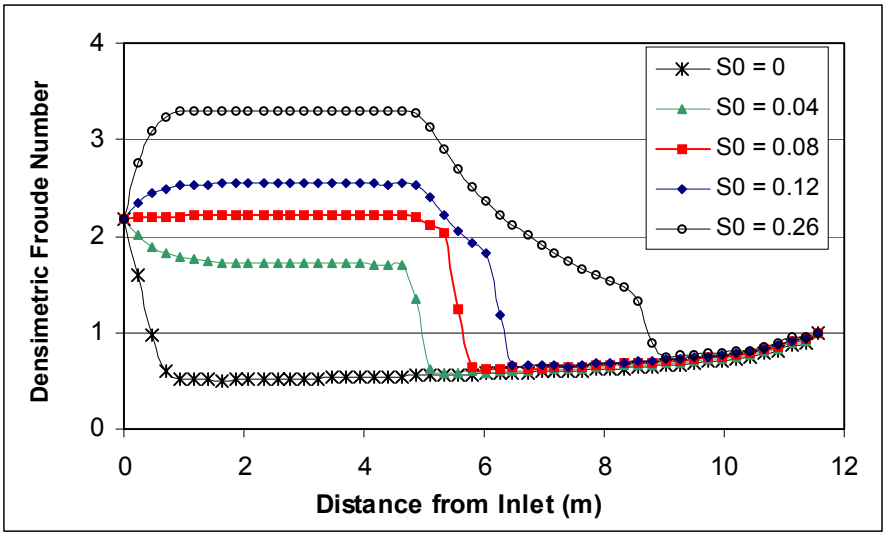
Densimetric Froude Number
Distance from Inlet (m)
S0 = 0
S0 = 0.04
S0 = 0.08
S0 = 0.12
S0 = 0.26
0
1
2
3
4
0
2
4
6
8
10
12

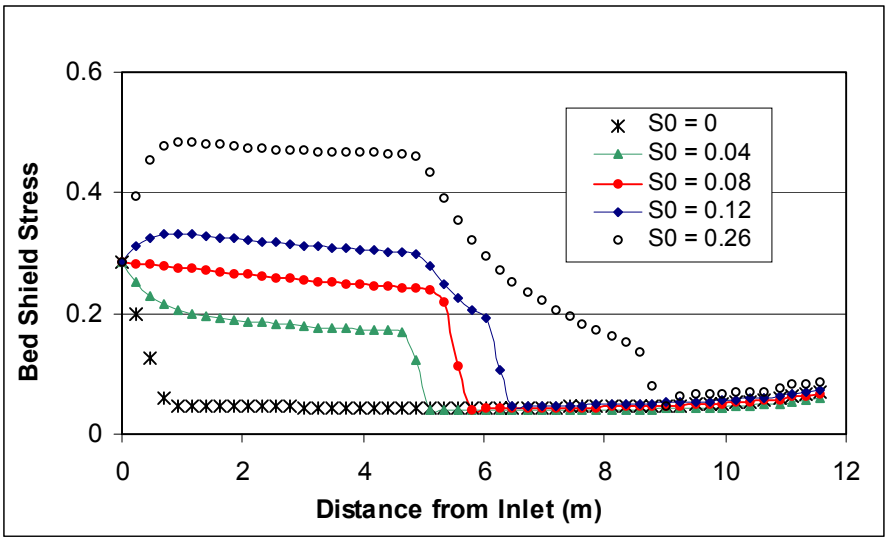
Bed Shield Stress
Distance from Inlet (m)
S0 = 0
S0 = 0.04
S0 = 0.08
S0 = 0.12
S0 = 0.26
0
0.2
0.4
0.6
0
2
4
6
8
10
12

Figure 8a, b, c

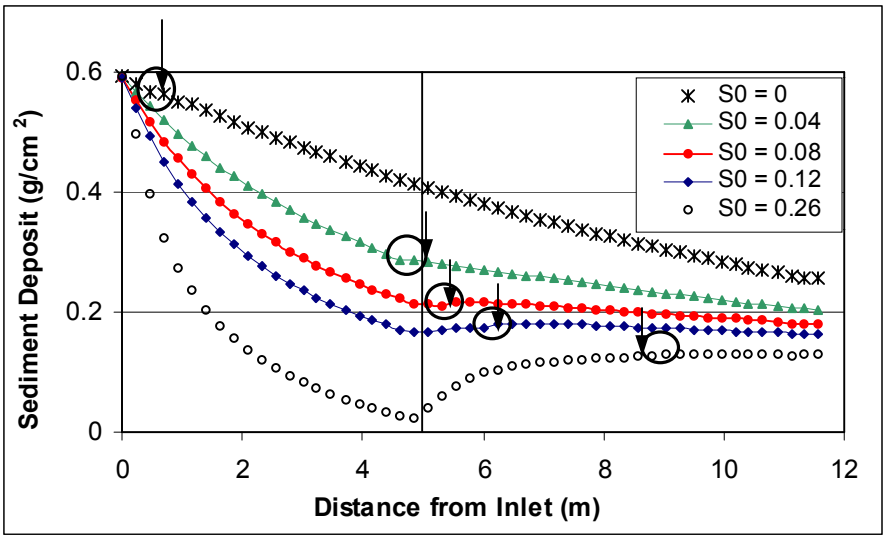
Sediment Deposit (g/cm 2)
0.6
0.4
0.2
0
0
2
4
6
8
10
12
Distance from Inlet (m)
S0 = 0
S0 = 0.04
S0 = 0.08
S0 = 0.12
S0 = 0.26

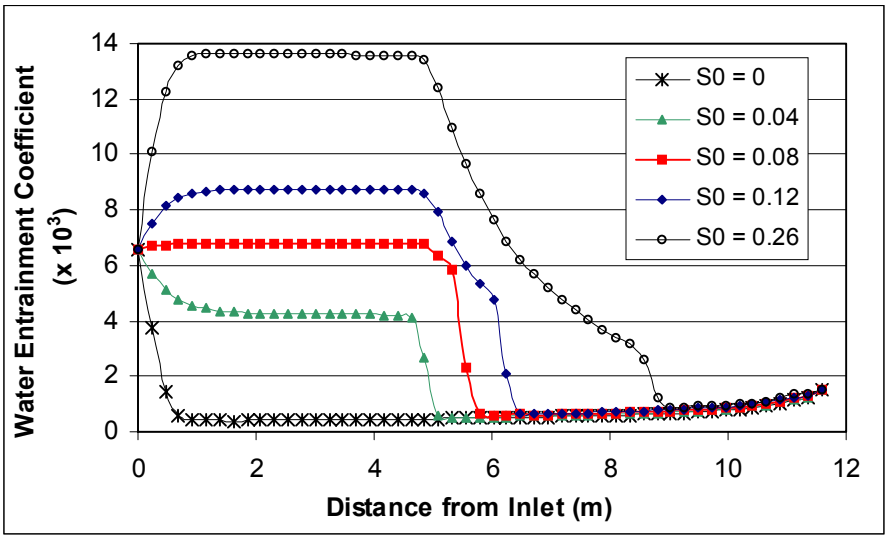
Water Entrainment Coefficient (x 10^3)
14
12
10
8
6
4
2
0
0
2
4
6
8
10
12
Distance from Inlet (m)
S0 = 0
S0 = 0.04
S0 = 0.08
S0 = 0.12
S0 = 0.26

Figure 8d,e

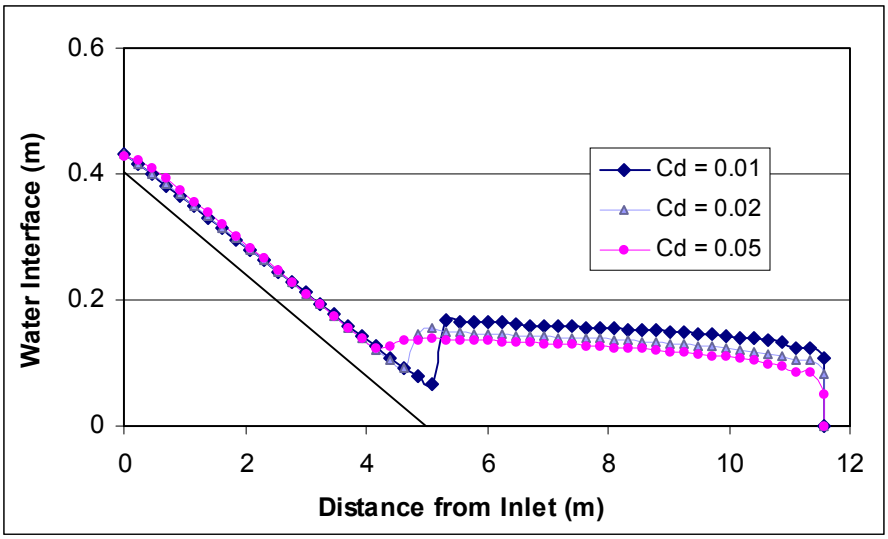
Water Interface (m)
0.6
0.4
0.2
0
0
2
4
6
8
10
12
Distance from Inlet (m)
Cd = 0.01
Cd = 0.02
Cd = 0.05

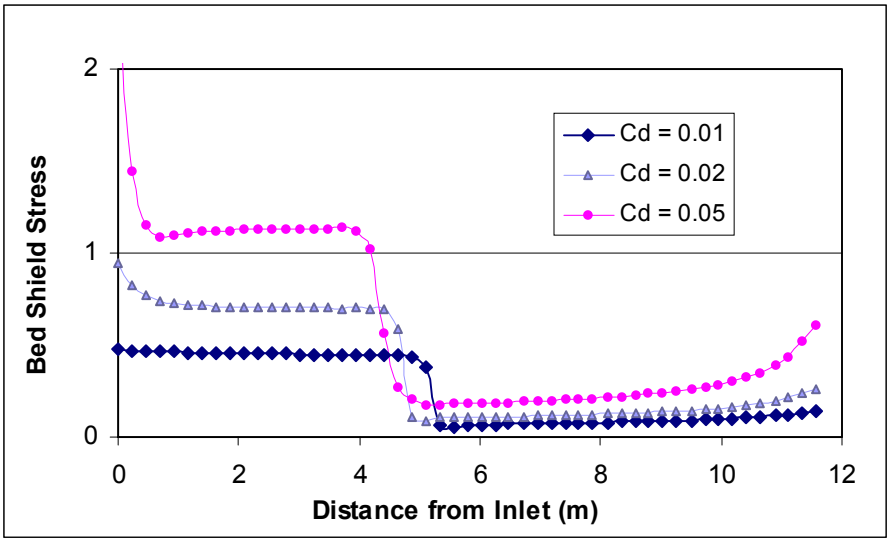
Bed Shield Stress
2
1
0
0
2
4
6
8
10
12
Distance from Inlet (m)
Cd = 0.01
Cd = 0.02
Cd = 0.05

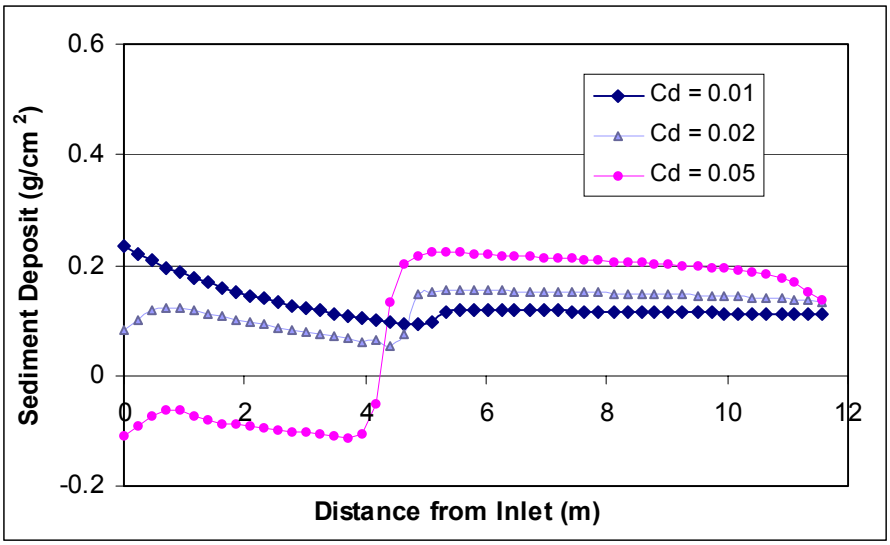
Sediment Deposit (g/cm 2)
0.6
0.4
0.2
0
-0.2
0
2
4
6
8
10
12
Distance from Inlet (m)
Cd = 0.01
Cd = 0.02
Cd = 0.05

Figure 9a, b, c

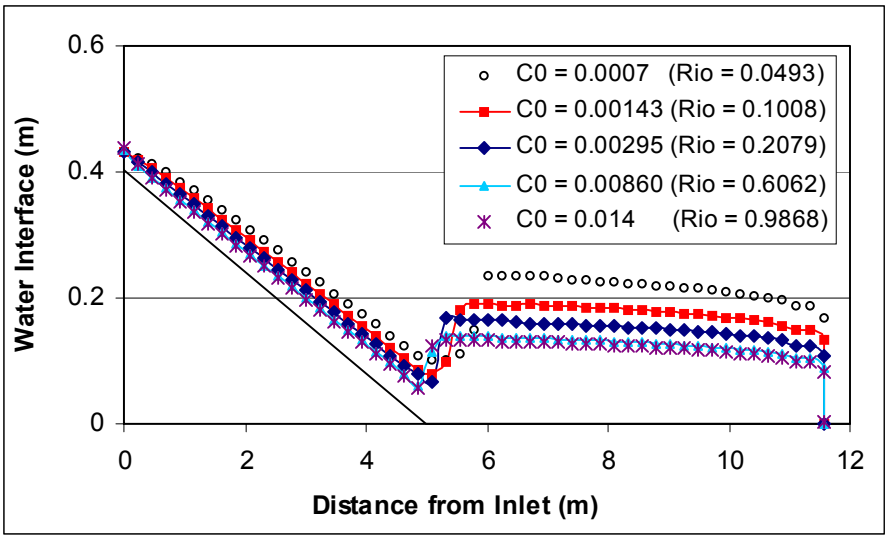

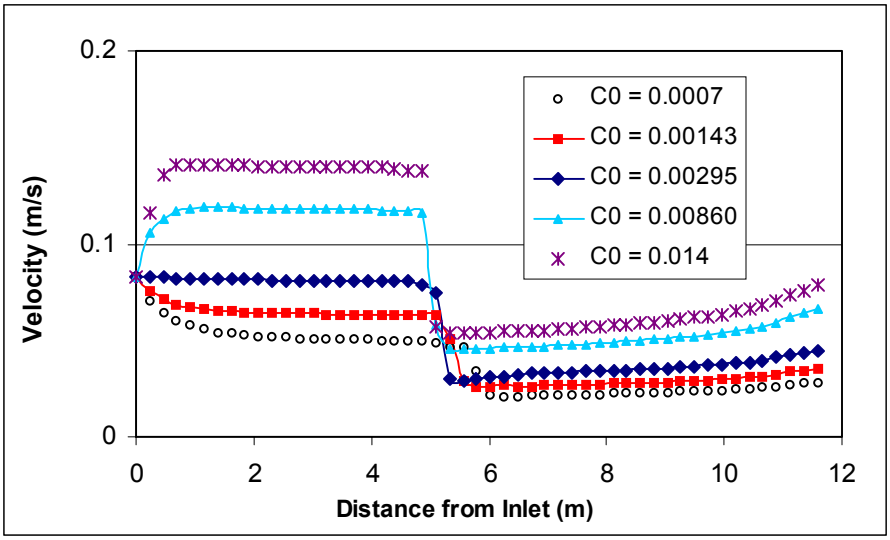

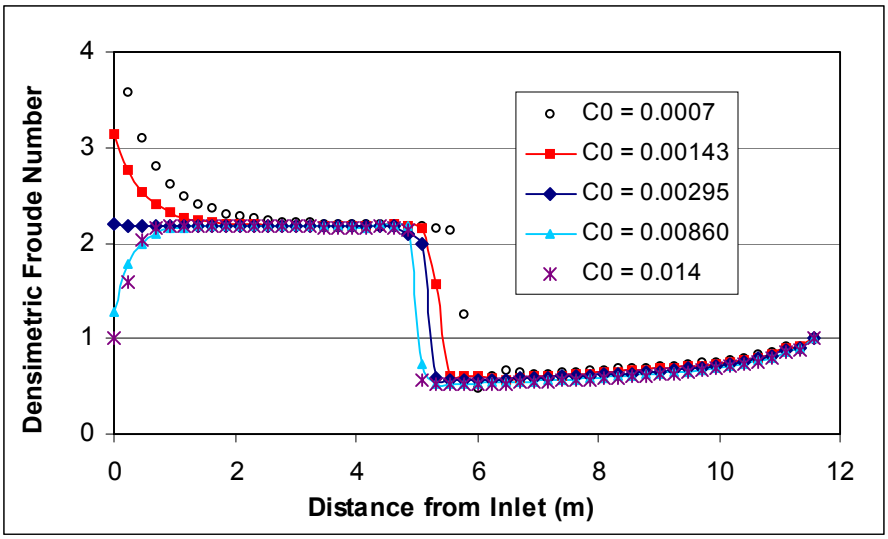

Figure 10a, b, c

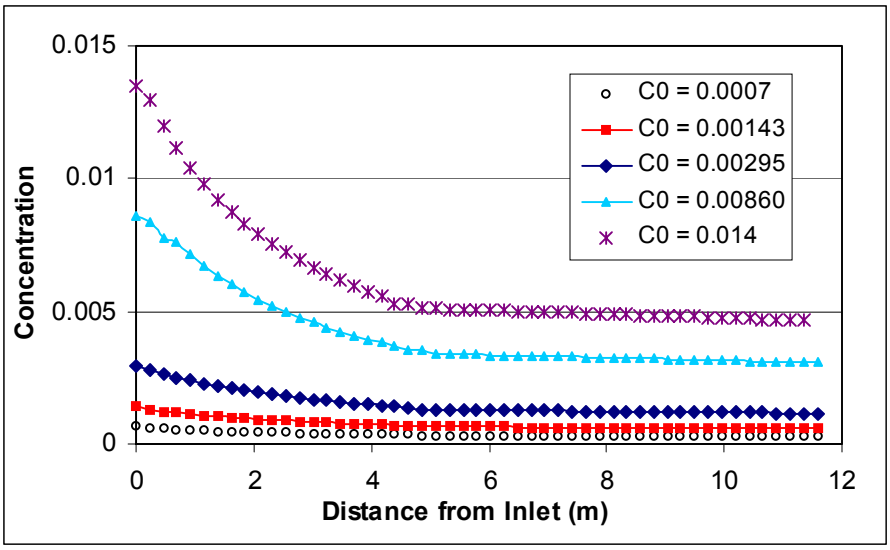
0.015
0.01
0.005
0
Concentration
0
2
4
6
8
10
12
Distance from Inlet (m)
C0 = 0.0007
C0 = 0.00143
C0 = 0.00295
C0 = 0.00860
C0 = 0.014

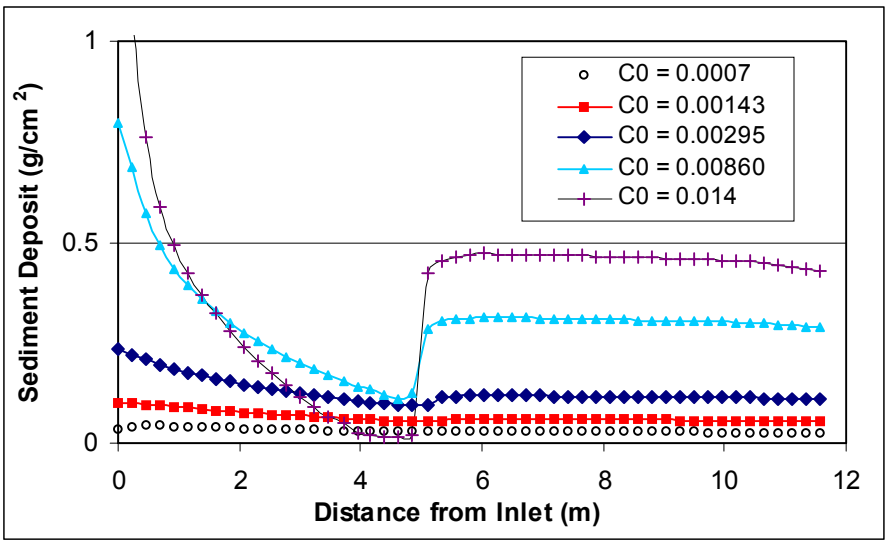
1
0.5
0
Sediment Deposit (g/cm 2)
0
2
4
6
8
10
12
Distance from Inlet (m)
C0 = 0.0007
C0 = 0.00143
C0 = 0.00295
C0 = 0.00860
C0 = 0.014

Figure 10d, e

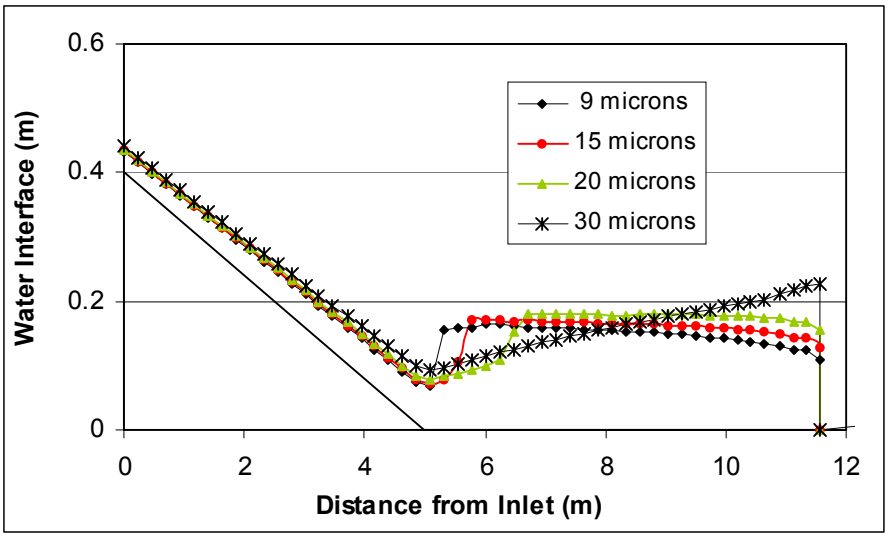

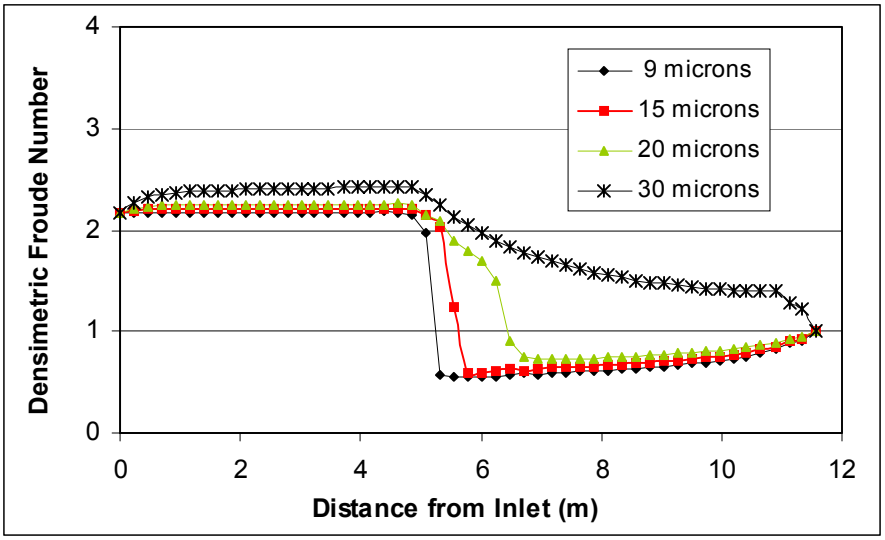

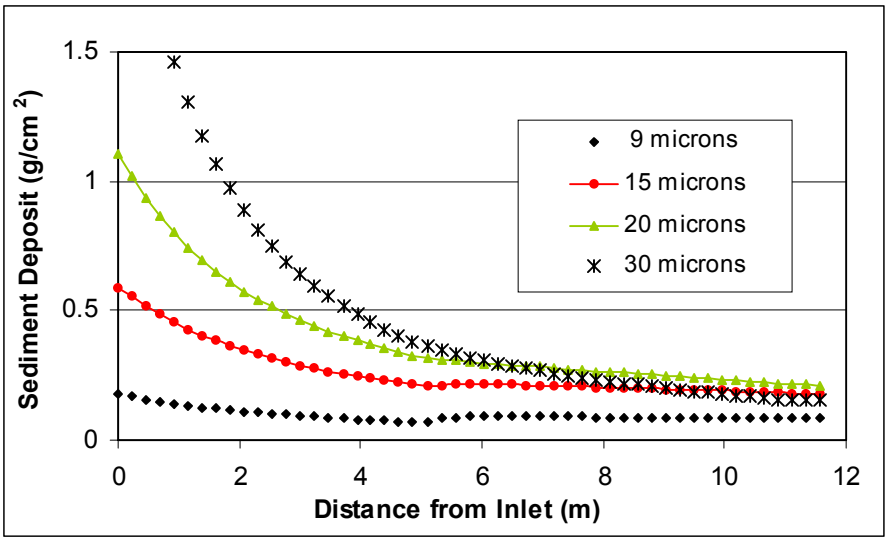

Figure 11a, b, c

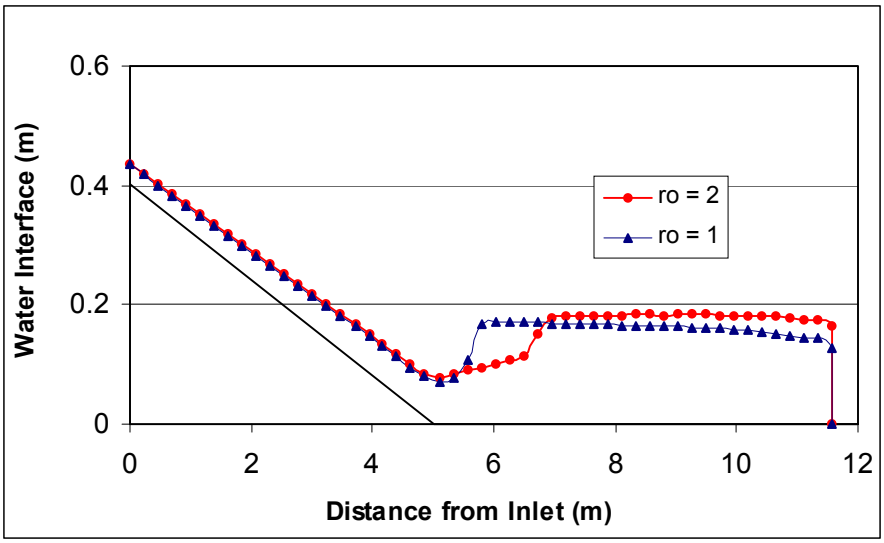

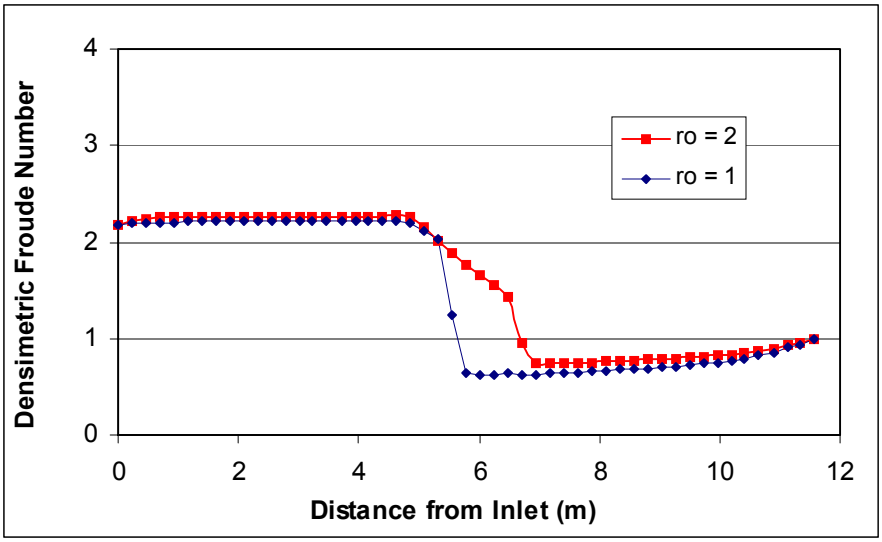

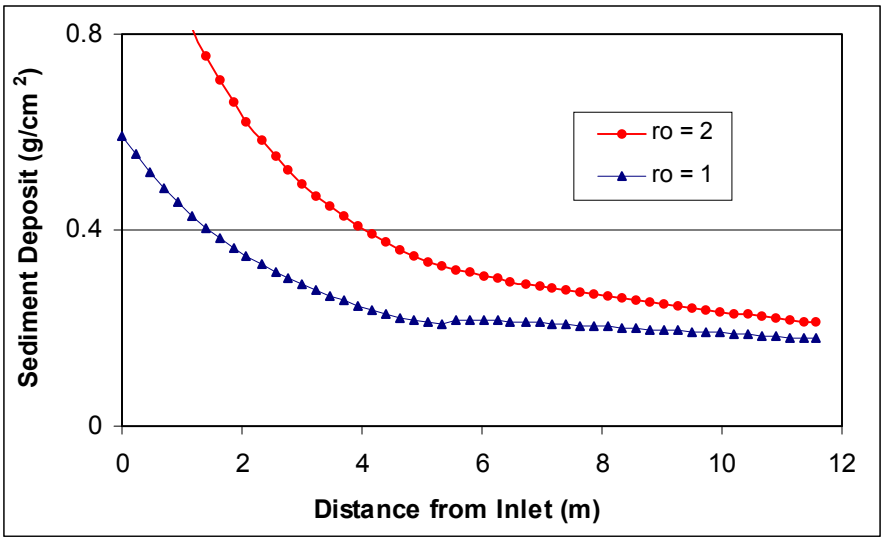

Figure 12a, b, c

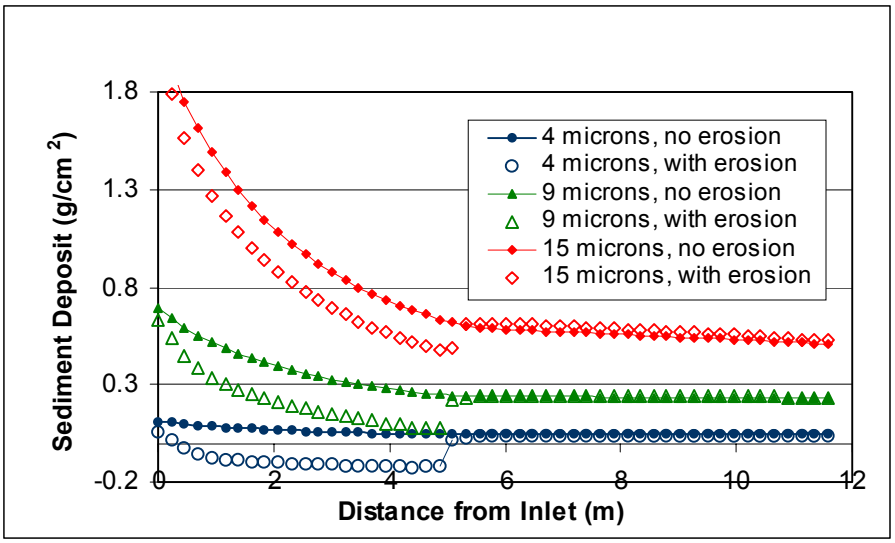

Figure 13

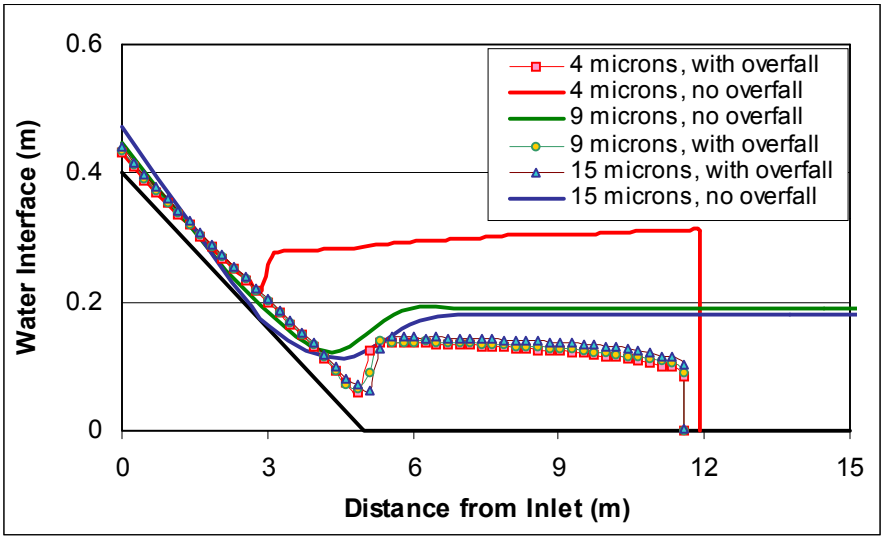

Figure 14

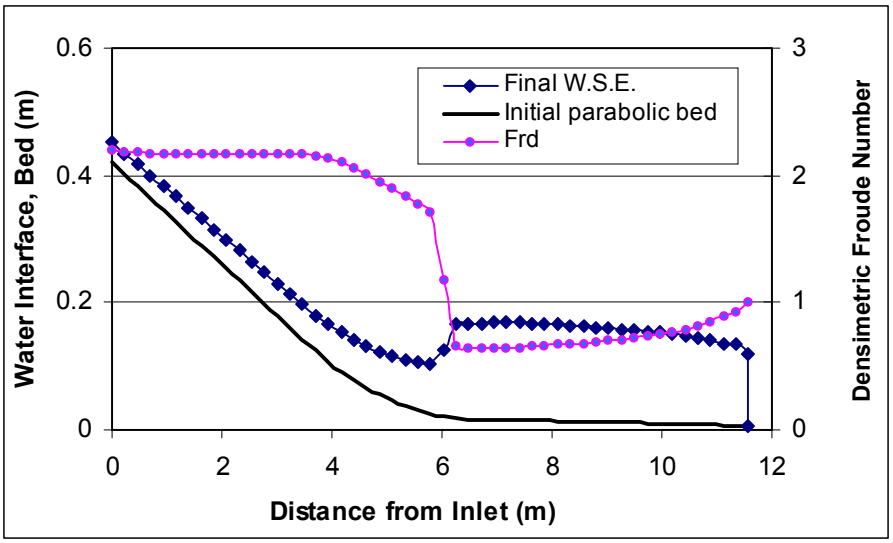
Final W.S.E.
Initial parabolic bed
Frd
Water Interface, Bed (m)
Densimetric Froude Number
Distance from Inlet (m)
0.6
0.4
0.2
0
3
2
1
0
0
2
4
6
8
10
12

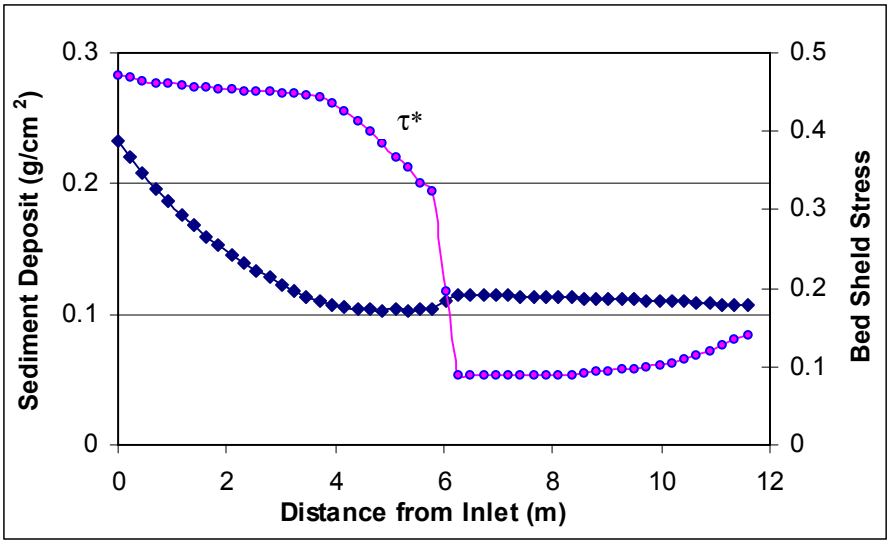
τ*
Sediment Deposit (g/cm 2)
Bed Sheld Stress
Distance from Inlet (m)
0.3
0.2
0.1
0
0.5
0.4
0.3
0.2
0.1
0
0
2
4
6
8
10
12

Figure 15a, b

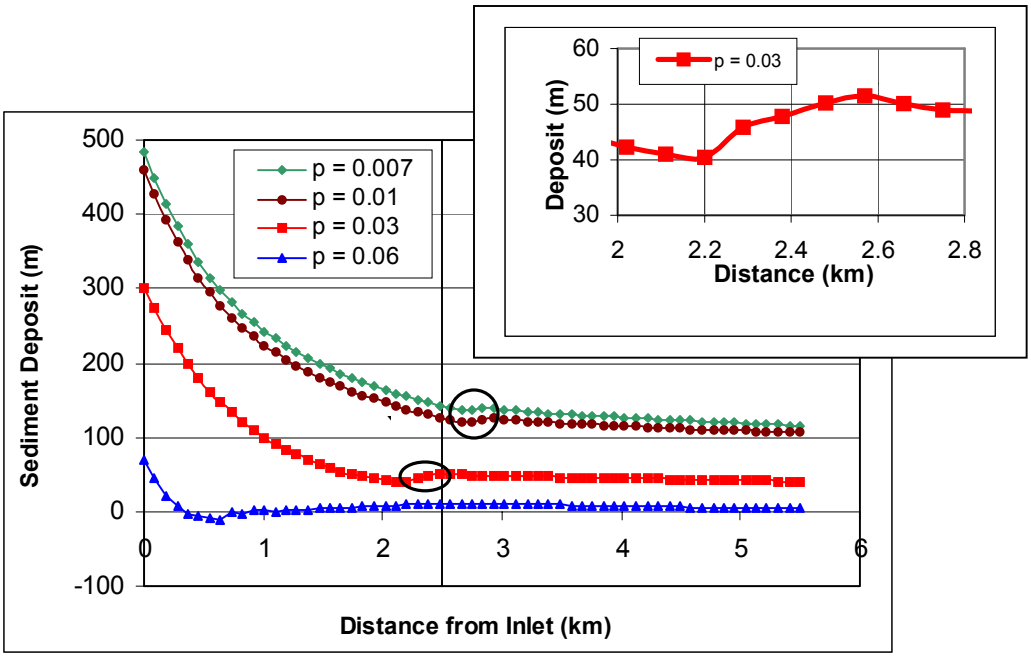

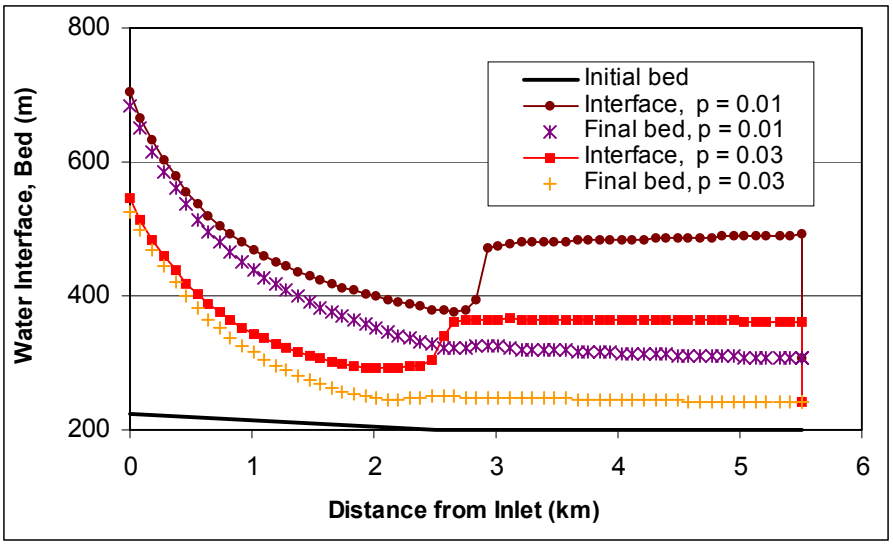

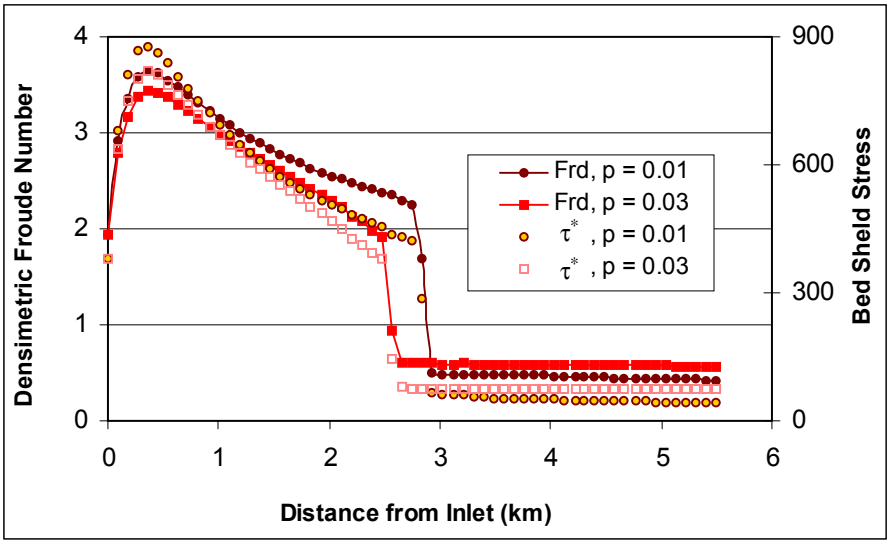

Figure 16a, b, c

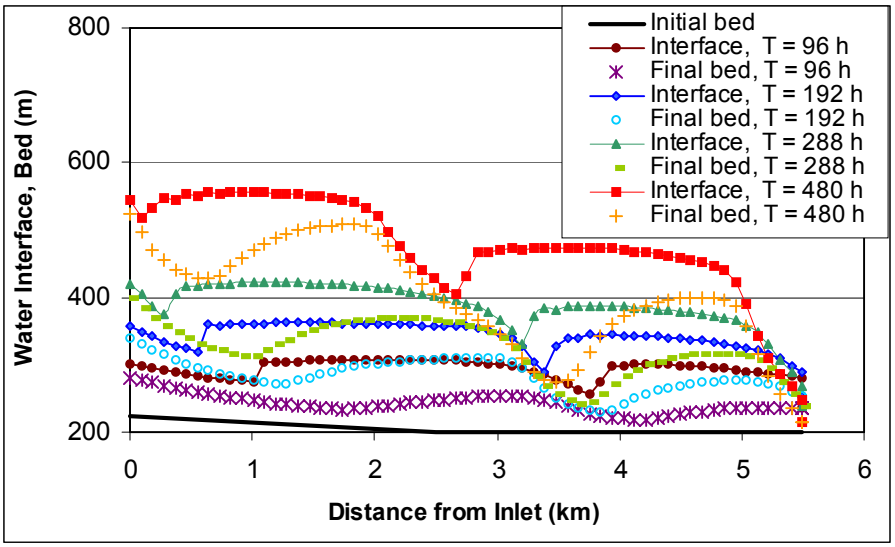
Initial bed
Interface, T = 96 h
Final bed, T = 96 h
Interface, T = 192 h
Final bed, T = 192 h
Interface, T = 288 h
Final bed, T = 288 h
Interface, T = 480 h
Final bed, T = 480 h
Water Interface, Bed (m)
800
600
400
200
0
1
2
3
4
5
6
Distance from Inlet (km)

Figure 17